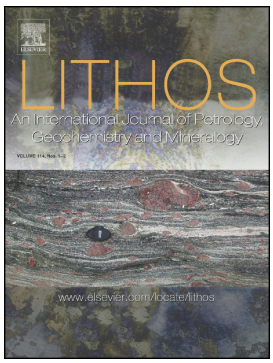

Age Progressive Volcanism Opposite Nazca Plate Motion: Insights from Seamounts and Drowned Islands on the Northeastern Margin of the Galápagos Platform

Christopher W. Sinton, Folkmar Hauff, Kaj Hoernle, Reinhard Werner

PII: S0024-4937(18)30141-5
DOI: doi:10.1016/j.lithos.2018.04.014
Reference: LITHOS 4630

To appear in:

Received date: 15 January 2018
Accepted date: 17 April 2018

Please cite this article as: Christopher W. Sinton, Folkmar Hauff, Kaj Hoernle, Reinhard Werner , Age Progressive Volcanism Opposite Nazca Plate Motion: Insights from Seamounts and Drowned Islands on the Northeastern Margin of the Galápagos Platform. The address for the corresponding author was captured as affiliation for all authors. Please check if appropriate. Lithos(2018), doi:10.1016/j.lithos.2018.04.014

Age Progressive Volcanism Opposite Nazca Plate Motion: Insights from Seamounts and Drowned Islands on the Northeastern Margin of the Galápagos Platform

Christopher W. Sinton[1*], Folkmar Hauff[2], Kaj Hoernle[2,3], and Reinhard Werner[2]

[1]Department of Environmental Studies and Sciences, Ithaca College, Ithaca, NY USA14850 csinton@ithaca.edu

[2] GEOMAR Helmholtz Centre for Ocean Research Kiel, Wischhofstraße 1-3, D-24148 Kiel, Germany

[3]Institute of Geosciences, University of Kiel, Ludewig-Meyn-Strasse 10, D-24118 Kiel, Germany

*corresponding author

Abstract

We present new geochemical and $^{40}Ar/^{39}Ar$ analyses from seven seamounts located off the northeastern margin of the shallow Galápagos Platform. Initial volcanism at 5.2 Ma created a small island (Pico) over the current location of the hotspot with geochemically enriched lavas. There is no further record of magmatism in the study area until 3.8 to 2.5 Ma, during which four roughly conical volcanoes (Sunray, Grande, Fitzroy, and Beagle) formed through ~~from~~ ~~the~~ eruption of lavas derived from a depleted mantle source. Sunray, Fitzroy, and Grande were islands that existed for ~3 m.y. ending with the submergence of Fitzroy at ~0.5 Ma. The youngest seamounts, Largo and Iguana, do not appear to have been subaerial and were active at 1.3 Ma and 0.5 Ma, respectively, with the style of edifice changing from the previous large cones to E-W elongate, composite structures. The progression of magmatism suggests that Pico erupted near 91.5°W near the location of the Galápagos plume while the others formed well east of the plume center. If the locations of initial volcanism are calculated using the eastward velocity of the Nazca plate, there appears to be a progression of younger volcanism toward the east, opposite what would be expected from a fixed mantle plume source. The rate that initial volcanism moves eastward is close to the plate velocity. A combination of higher temperature and geochemical enrichment of the thickened lithosphere of the Galápagos platform could have provided a viscosity gradient at the boundary between the thick lithosphere and the thinner oceanic lithosphere to the northeast. As this boundary moved eastward with the Nazca plate, it progressively triggered shear-driven mantle upwelling and volcanism.

1. Introduction

The Galápagos magmatic province in the eastern Pacific consists of subaerial volcanoes that

form the well-known islands and a variety of submarine volcanic features (Figure 1). Several characteristics of this province adhere to the "classic" hotspot model, such as a well-defined volcanic center with a chain of extinct islands extending in the direction of motion of the Cocos and Nazca Plates (Morgan, 1972). The westernmost islands of Fernandina and Isabela are the most active, have compositions consistent with a deep mantle source (Kurz and Geist, 1999; White et al., 1993), and lie over a low velocity mantle zone (Byrnes et al., 2015; Geist et al., 2005; Hooft et al., 2003; Villagómez et al., 2014) that represents a mantle plume. To the east of Fernandina, there is a general increase in the oldest ages of the islands and seamounts (White et al., 1993), consistent with the hotspot model. Despite these characteristics, there are several observations that do not support a simple hotspot model. While the oldest ages do increase to the east, significant magmatism on the islands can persist hundreds of kilometers from Fernandina. For example, young, relatively recent lavas are found 200 km east of Isla Fernandina on Isla San Cristobal (Geist et al., 1986; White et al., 1993). There also is recent (<1 Ma) magmatism to the north of the main platform between the inferred center of the hotspot and the Galápagos Spreading Center (GSC). This set of volcanoes is collectively referred to as the Northern Galápagos Volcanic Province (NGVP) and include five young islands (Wolf, Darwin, Pinta, Marchena, and Genovesa) (Harpp et al., 2002; White et al., 1993) and a collection of seamounts distributed along several volcanic lineaments arrayed in a fan-shaped pattern (Mittelstaedt et al., 2012; Sinton et al., 2003) (Figure 1). The volcanism of the NGVP is likely a result of the interactions between the GSC and the hotspot and there are several models that attempt to explain this relationship (Harpp and Geist, 2002; Mittal and Richards, 2017; Mittelstaedt et al., 2014; Mittelstaedt and Ito, 2005; Morgan, 1978; Sinton et al., 2003).

While the current NGVP represents the more recent (<1 Ma) interaction between the GSC and the Galápagos hotspot, to determine if this pattern of volcanism has been a characteristic of the region in the past we need to examine the Northeast Seamounts, a distinct collection of volcanoes that lie to the northeast of San Cristobal and are separated from the main, shallow platform by ~2000m depth. These seamounts were mapped and sampled during Leg 2 of the 1990 PLUME2 expedition of the *R/V Thomas Washington* and during the 2001 SO158 MEGAPRINT expedition of the *R/V Sonne*. Major- and trace element data of four glass samples from MEGAPRINT are reported by Peterson et al. (2017). Data from PLUME2 have been reported previously including limited trace element and Sr-Nd-Pb isotopic ratios (Harpp and

White, 2001), $^{3}He/^{4}He$ ratios (Graham et al., 1993), major and trace geochemistry (Sinton et al., 2014) and radiometric dating (Christie et al., 1992; Sinton et al., 1996). However, since the original radiometric ages were reported, more precise mass spectrometers and low-blank extraction systems have been built to better analyze the low K_2O, young basalts that characterize this region. In this paper, we report new radiometric age and geochemical analyses from both cruises and then use the new data to constrain the temporal and tectonic evolution of the Northeast Seamounts.

2. Seamount and Sample Descriptions

There are at least seven identified seamounts in the region northeast of the relatively shallow Galápagos Platform (Figure 1). Four of the seamounts were mapped using multibeam sonar and dredged at seven sites during PLUME2 and three other seamounts were partly mapped and sampled during MEGAPRINT. Sunray and Fitzroy were named during PLUME2 and here we give names to the others. Descriptions of the morphology and petrology of the dredged samples from PLUME2 are published in detail elsewhere (Sinton, 1992; Sinton et al., 2014). Dredge site locations and general rock descriptions for each seamount are reported in Table 1 and relevant details are described below.

Sunray Seamount is a truncated cone with a 20 km basal diameter that rises from a depth of ~2000 meters below sea level (mbsl) to a ~9 km diameter flat-topped peak 370 mbsl. It was sampled at two sites during PLUME2 (PL2-9 and -10). Recovered rocks include glassy, vesicular pillow basalts (often with small olivine and Al-rich spinel phenocrysts) and weathered, plagioclase-phyric pillow basalts. These make up five distinct lava groups based on petrology and geochemistry (Sinton et al., 2014) (Table 1). To the northeast of Sunray lies an E-W elongated seamount with a peak depth of 1215 mbsl and is ~20 km in length. This seamount, which we are calling Iguana, was sampled at site DR83 during MEGAPRINT, recovering 11 aphyric basalt fragments, some with small pockets of fresh glass. The basalt fragments have thick alteration haloes with fresh interiors.

Fitzroy Seamount is another truncated cone that rises from a ~25 km diameter base at ~2300 mbsl to a ~10 km diameter flat top at 200 mbsl. During PLUME2, Fitzroy was sampled at sites PL2-11 and -12, recovering aphyric basalts, olivine-plagioclase phyric basalts and plagioclase

ultraphyric basalts (Sinton et al., 2014). Its flat top and the recovery of rounded cobbles indicate that the seamount had experienced subaerial erosion and is likely a drowned island (Christie et al., 1992). Aligned to the northeast of Fitzroy is a small ~500 m tall volcanic cone and then a larger seamount with a ~16 km basal diameter at ~2500 m rising to ~800 mbsl. This seamount, here named Beagle Seamount, was dredged on its northeastern flank at site DR80 during MEGAPRINT, which recovered six aphyric basalt fragments with Mn-crusts.

Largo Seamount is a ~42 km long composite structure that trends roughly E-W with a peak that lies ~700 m below sea level. It was sampled at two locations (PL2-13 and -14) during PLUME2 and two sites (DR72 and DR72A) on the western flank during MEGAPRINT. Dredged rocks from the PLUME2 sites include aphyric, plagioclase-olivine phyric, and plagioclase ultraphyric basalts that all have very depleted geochemical compositions (Sinton et al., 2014, 1993). The dredges on the western end of Largo at sites DR72 and DR72A recovered fresh, aphyric and non-vesicular pillow basalt fragments with glassy rims.

Grande Seamount lies to the southwest of Largo Seamount. Its roughly circular base has a diameter of ~30 km and rises from ~2000 mbsl to a somewhat flat peak that is at ~250 mbsl and approximately 5 km across. It was dredged during MEGAPRINT at one site (DR73) near the base of the northern flank, recovering six variably-altered aphyric basalt fragments, some with Mn-crusts, and a clastic sediment cobble.

Pico Seamount is the westernmost of the volcanoes of this study and it lies due north of Isla San Cristobal. It is a cone with a ~12 km basal diameter and a slightly rounded top. The peak rises to ~800 mbsl from the 1400-1550 mbsl seafloor around it. This seamount was sampled at dredge site PL2-16, which recovered three basalt clasts with Mn coatings but no glass.

3. Methods

3.1 Major and Trace Element Analysis

Major elements of whole rock powders for five MEGAPRINT samples (Grande, Beagle, western flank of Largo, and Iguana) were determined on fused beads on a Philips X'unique PW 1480 X-ray fluorescence spectrometer (XRF) at GEOMAR. Rock standards JA-2, JB-2 and JB-3 measured along with the samples lie within 5% of the working values of Govindaraju (1994) except MnO (6%) and P_2O_5 (7%) for JB-3. Major elements for PL2-16-3 (Pico) were determined

using the Philips PW2404 XRF spectrometer at Colgate University with methods described in Sinton et al. (2014). Trace elements for the MEGAPRINT samples were measured on an Agilent 7500 ICP-MS at the Institute of Geosciences (Kiel University) after the methods of Garbe-Schönberg (1993). When compared to GEOREM reference values (Jochum et al., 2016) the accuracy of rock standards prepared along with the samples lie within 5%, except Ta (9%) for BHVO-1 and within 9% for BIR-1 except Ta (12%), Th (11%) and U (15%) (see Appendix). Trace elements for sample PL2-16-3 were determined using the Thermo Fisher iCAPQ at Middlebury College (Vermont). Solutions were prepared by fusing 0.2g of sample with 1.8g lithium metaborate flux in a platinum crucible at 1050^{o}C. The melt was then dissolved in ultrapure 5% HNO_3. Cs, Re and Rh internal standard spikes were added and solutions were diluted with ultrapure 5% HNO_3 to 1000x to analyze Sc, La, Ce, Pr, Nd, Sm, Eu, Gd, Tb, Dy, Ho, Er, Tm, Yb, Lu, Th and U and 2000x solution was used to analyze V, Cr, Co, Ni, Cu, Zn, Rb, Sr, Y, Zr, Nb, Ba, Hf, Ta, and Pb. Quality control samples were run after every five samples. Calibration curves, used to calculate elemental concentrations in unknowns, were constructed from analyses of synthetic standards, including blank, 2.5 ppb, 5.0 ppb, 10.0 ppb, and 50.0 ppb solutions and BCR-2 was analyzed as an unknown.

3.2 Sr-Nd-Pb Isotope Analysis

Sr-Nd-Pb isotope analyses were performed on one glass sample (DR72-3) and five whole rock samples (DR72-1, 72a-1, 73-4, 80-1, and 83-1) recovered during MEGAPRINT. All samples were leached in 2N HCl at 70°C for 30 minutes and rinsed three times with ultrapure (u.p.) water prior to dissolution in a 5:1 mixture of concentrated HF u.p and HNO_3 u.p. The element chromatography followed the methods outlined in Hoernle et al. (2008). Sr-Nd isotopic ratios were determined on a TRITON thermal ionization mass spectrometer (TIMS) and Pb isotopes on a MAT262 RPQ2+ TIMS at GEOMAR. Sr and Nd isotopic ratios are normalized to $^{86}Sr/^{88}Sr$= 0.1194 and $^{146}Nd/^{144}Nd$= 0.7219 respectively. External errors reported below are 2SD. NBS987 gave $^{87}Sr/^{86}Sr$ = 0.710251 ± 0.000011 (N=44) and La Jolla $^{143}Nd/^{144}Nd$= 0.511845 ± 0.000006 (N=68). NBS981 (N=37) gave $^{206}Pb/^{204}Pb$ = 16.899 ± 0.007, $^{207}Pb/^{204}Pb$ = 15.436 ± 0.008, $^{208}Pb/^{204}Pb$ = 36.525 ± 0.026. The measured NBS981 values are mass bias corrected to NBS981 Double Spike (DS) values of Hoernle et al. (2011) and the adjustment factored into the sample data. Total chemistry blanks were <100 pg for Sr, Nd and Pb and thus considered negligible. A

subset of five whole rock samples (PL2-9-50, 11-7, 12-5, 12-7, and 13-34) from PLUME2 have been recently analyzed for Sr-Nd and Pb-DS on the TRITON Plus at GEOMAR. The sample data is reported relative to $^{87}Sr/^{86}Sr = 0.710250 \pm 0.000006$ (N=7) for NBS987 and La Jolla $^{143}Nd/^{144}Nd = 0.511850 \pm 0.000004$ (N=5). Long term DS corrected NBS981 values are $^{206}Pb/^{204}Pb = 16.9407 \pm 0.0019$, $^{207}Pb/^{204}Pb = 15.4977 \pm 0.0019$ and $^{208}Pb/^{204}Pb = 36.7199 \pm 0.0047$ (N=78, since 2015).

3.3 $^{40}Ar/^{39}Ar$ Age Analysis

$^{40}Ar/^{39}Ar$ step heating analysis was used to determine the eruptions ages of the Northeast Seamount samples. However, using dating techniques based on the decay of ^{40}K to ^{40}Ar to analyze the young (<5Ma) submarine basalts in this region is a challenge because of the low K_2O content of the mostly tholeiitic and often primitive lavas that were recovered. In fact, some of the rock samples, particularly those from site PL2-14 and D72/72a (Largo Seamount), have such low K_2O (<0.10% wt.) that they are unsuitable for $^{40}Ar/^{39}Ar$ analyses because there would be insufficient ^{40}K to generate measurable radiogenic ^{40}Ar. From Largo Seamount, only PL2-13-4 had K_2O content (0.11% wt.) above our cutoff of 0.10%.

For all the analyses, material was taken from the least altered interiors of the recovered rocks then crushed to a 210–300 µm fraction. All crushed material was cleaned by a series of acid leaching steps in an ultrasonic bath as follows: 1N HCl (60 min), 6N HCl (60 min), and 1N HNO_3 (60 min). This was followed by ultrasonic cleaning in ultrapure deionized water and handpicking under a binocular microscope to remove any altered grains and phenocrysts. In this study, only groundmass separates free of phenocrysts were used because olivine and plagioclase phenocrysts, particularly those with melt inclusions, often contain excess (mantle-derived) ^{40}Ar that could result in an apparent age that is older than the actual crystallization age (Sharp and Renne, 2005). Groundmass is also preferred to plagioclase phenocrysts for submarine basalts because, in general, the groundmass has more K_2O than the plagioclase (Duncan and Hogan, 1994).

$^{40}Ar/^{39}Ar$ radiometric dating was conducted at Oregon State University (OSU) according to the procedures described in Koppers et al. (2011). The exception was sample PL2-16-3 which was analyzed at the geochronology lab at Lamont-Doherty Earth Observatory (LDEO).

Approximately 100 mg of each cleaned sample was wrapped in an aluminum foil disk and placed in a vacuum-sealed quartz glass tube with aliquots of the FCT-3 biotite flux monitor (28.03 ± 0.18 Ma, 1σ; (Renne et al., 1998) placed at intermittent heights. Irradiated samples were incrementally heated by scanning a defocused CO_2 laser. Mass analysis at OSU was completed using a Thermo Scientific Model ARGUS VI multi-collector mass spectrometer and mass analysis at LDEO was done using a Micromass VG 5400 instrument. After measuring all heating steps, plateau ages and isochron ages were calculated as weighted means with $1/\sigma^2$ as weighting factor (Taylor, 1997) and as YORK2 least squares fits with correlated errors (York, 1968) using the ArArCALC software from Koppers (2002). All ages were calculated using the decay constant of $5.530 \pm 0.097 \times 10^{-10}$ 1/yr (2σ) as reported by Min et al. (2000). Reported errors on the $^{40}Ar/^{39}Ar$ ages are at the 95% confidence level (2σ) including 0.3–0.4% standard deviation in the J-value.

4. Results

4.1 Major, Trace, and Sr-Nd-Pb Isotope Results

Sinton et al. (2014) noted that the Northeast Seamount lava compositions from the PLUME2 dredges fall into three general categories: 1) the light rare earth element (LREE) enriched and isotopically enriched sample from Pico (PL2-16-3); 2) very slightly LREE-enriched basalt groups from Sunray (PL2-9-50) and Fitzroy (PL2-11-5); and 3) incompatible trace element depleted tholeiitic basalts that characterize Largo (PL2-13 and -14) and the remaining lavas of Sunray and Fitzroy. Multi incompatible (or spider) element diagrams (Figure 2) of the new data normalized to primitive mantle show that the MEGAPRINT lavas from Grande, the western flank of Largo, Beagle, and Iguana all fall under the third category of depleted tholeiites. In Figure 2A the depleted lavas show a pronounced positive Sr anomaly with the exception of the one sample from Grande Seamount.

The new isotopic analyses for samples from Grande, the western flank of Largo, Beagle, and Iguana show depleted signatures with $^{87}Sr/^{86}Sr$ ranging from 0.7025 to 0.7026, εNd = 9.20-9.97, $^{206}Pb/^{204}Pb$ = 18.34-18.67, $^{207}Pb/^{204}Pb$ = 15.50-15.52, and $^{208}Pb/^{204}Pb$ = 37.83-38.11 (Figure 3). The new isotopic analysis of PLUME2 samples were done to fill in data gaps as there were no analyses from the trace element enriched Sunray group nor the depleted lava group from site PL2-11 on Fitzroy and to reanalyze samples from Fitzroy (PL2-12) and Largo (PL2-13) reported

by Harpp and White (2003) that appeared to have been affected by uncontrolled Pb isotopic fractionation. These data are now also consistent with derivation from a depleted mantle source.

4.2 $^{40}Ar/^{39}Ar$ radiometric dating

The results from the $^{40}Ar/^{39}Ar$ analyses are presented in Table 3 and plots of the step-age plateaus are shown in Figure 4. We use the following accepted criteria (Koppers et al., 2011; Lanphere and Dalrymple, 1976; Pringle, 1993) to determine the reliability of the $^{40}Ar/^{39}Ar$ ages:

- High-temperature plateaus in the age spectra should include more than three incremental heating steps and at least 50% of the total amount of $^{39}Ar_K$ released;
- the age step plateau and isochron ages should be concordant at the 95% confidence level;
- the $^{40}Ar/^{36}Ar$ intercepts on the isochron diagrams should be concordant with the atmospheric value of 295.5 at the 95% confidence level;
- the mean square of weighted deviations (MSWD) (Roddick, 1978; York, 1968) for age step plateau and isochron ages should be (<2) when compared to student's t test and F statistic critical values for significance, respectively.

Ten analyzed samples gave reliable age information (Table 3 and Figure 4) that meet the above criteria. Pico Seamount (PL2-16-3) was analyzed in duplicate (same irradiation, separate aliquots) with both analyses indicating excess ^{40}Ar with initial $^{40}Ar/^{36}Ar$ from the isochrons above the atmospheric value of 295.5. Both samples have step ages recalculated with the respective initial $^{40}Ar/^{36}Ar$ ratios determined from the isochrons and these spectra and plateau ages are shown in Figure 4. The two plateau ages from Pico are averaged to give an age of 5.2 ± 0.5 Ma which is concordant with the isochron ages (Table 3).

5. Discussion

5.1 Comparison to Prior Age Data

To use the age data to constrain the magmatic and tectonic history of the Northeast Seamounts, we need to first compare the new $^{40}Ar/^{39}Ar$ ages to those previously reported for Sunray, Fitzroy, and Pico Seamounts by Sinton et al. (1996) (Table 4). For Sunray, the 3.1 ± 0.1 Ma $^{40}Ar/^{39}Ar$ plateau age reported in this study is younger than the previous 5.7 ± 1.2 Ma (2σ error) and the 3.8 ± 0.1 Ma ^{40}Ar-^{39}Ar plateau age for PL2-10-5 reported here is younger than the previous age of 5.6 ± 2.8 Ma. For Fitzroy, the three new $^{40}Ar/^{39}Ar$ plateau ages from both dredge sites are

between 1.7 ± 0.2 Ma to 2.5 ± 0.1 Ma are younger than 3.2 ± 1.0 Ma (2σ error) age from PL2-11 reported by Sinton et al. (1996). In these instances, the new ages are consistently lower and more precise than those previously reported. For Pico Seamount (PL2-16), the age reported here of 5.2 ± 0.5 Ma for PL2-16-3 is within the uncertainty of the 5.6 ± 0.6 Ma (2σ error) previously reported for sample PL2-16-2.

The overall pattern is that the younger, somewhat more depleted samples from Fitzroy and Sunray have systematically younger and more precise ages compared to the previously published analyses whereas the more enriched and older Pico samples have similar ages. This could be explained by a combination of better sample preparation and newer analytical equipment. The $^{40}Ar/^{39}Ar$ method is based on the decay of ^{40}K to ^{40}Ar (half-life 1.251 x 10^9 m.y.) so young lavas with low K_2O like those from Sunray and Fitzroy did not have time to generate much radiogenic ^{40}Ar. The prior analyses were done using a system with a high volume (and therefore a high blank) extraction system with sample heating done with an induction coil and a large sample holder so the low amount of radiogenic ^{40}Ar from these samples could have been drowned by the atmospheric component (Duncan and Hogan, 1994). In addition, the mass analysis was done with a low-sensitivity mass analyzer (MS10S) with mass peaks recorded by a stylus on paper. The newer ARGUS system uses a much more precise mass analyzer to measure gas from a very small, low-blank, all-metal extraction system and sample heating was done by laser. Finally, the sample preparation used in the earlier study was not as rigorous as the one employed in this work, specifically, the acid leaching steps were not followed and phenocrysts that may contain excess ^{40}Ar were not removed. It is not clear which of these variables led to a decrease in the measured ages from Sunray and Fitzroy, but the result is that we use only the new age data for these seamounts in the discussion. Our results suggest that older studies reporting ^{40}Ar-^{39}Ar analyses of young (< 5 Ma), low K_2O (< 0.2%) lavas should be reassessed and perhaps reanalyzed.

5.2 Mantle Sources and Petrogenetic Processes

Prior isotopic studies of Galápagos volcanism have identified multiple distinct mantle sources (e.g., Blichert-Toft and White, 2001; Harpp and White, 2001; Hoernle et al., 2000; Kurz and Geist, 1999; White et al., 1993): 1) An enriched central Galápagos domain (CGD or PLUME) source common to the central-western Galápagos volcanoes that make up Fernandina and most

of Isabela; 2) An enriched southern domain (SGD and FLO) component that characterizes Floreana that has more radiogenic Pb isotopic ratios than CGD; 2) a Northern Galápagos Domain (NGD or WD) component that is evident in the northwestern islands of Wolf and Darwin and is distinguished by having elevated and $^{208}Pb/^{204}Pb$ at a given and $^{206}Pb/^{204}Pb$ ratio; and 4) a depleted eastern Galápagos domain (EGD or DGM) with relatively unradiogenic isotopic ratios similar to the depleted upper mantle. A combined Sr-Nd-Pb isotopic dataset that includes our new data and those reported by Harpp and White (2003) show that all the Northeast Seamount lavas except for the Pico sample are derived from a depleted mantle source and fall within or near the EGD (Figure 3). Helium isotopic analysis from Sunray, Fitzroy, and Largo are consistent with this conclusion (Graham et al., 1993). Pico has consistently more radiogenic isotopic ratios that fall within the CGD.

Within the field of depleted lavas, the plot of $^{87}Sr/^{86}Sr$ vs εNd (Figure 3a) shows a relatively narrow range of high εNd except PL2-9-50, one of the slightly trace element enriched Sunray lavas, has a slightly lower value. $^{87}Sr/^{86}Sr$ for some samples is in the lower range of EGD, but several samples trend toward increasing values at a given εNd. This could be a due to incorporation of seawater or it could be due to interaction with the lithosphere. Saal et al. (2007) noted that many Galápagos island and seamount lavas that erupted east of 91.5°W show a similar trend in $^{87}Sr/^{86}Sr$ combined with a positive Sr anomaly. They attributed this to interactions of the melt with plagioclase cumulate during ascent in the lithosphere. While this could explain both the higher $^{87}Sr/^{86}Sr$ and positive Sr anomalies (Figure 2) that characterize most of the depleted Northeast Seamount lavas, not all of the samples with a positive Sr anomaly have higher $^{87}Sr/^{86}Sr$ ratios than expected. In any case, we do not use the Sr isotopic ratios to constrain mantle source(s).

Incompatible trace element ratios may be used to help constrain the degree of partial melting. La is more incompatible than Sm, so La/Sm_n ratios can be used as an indicator for the degree of partial melting assuming that the mantle source has a constant La/Sm_n. Figure 5 shows that there are three general groups in La/Sm_n from highest to lowest: 1) Pico; 2) the slightly incompatible element enriched lavas from Fitzroy (PL2-11-5) and Sunray (9-50, -56, -65); and 3) the remaining lavas with ratios between 0.2 to 0.6. The middle group generally have depleted Nd-Pb

isotopic ratios but have very slightly higher radiogenic $^{207}Pb/^{204}Pb$ and 9-50 has slightly more radiogenic εNd compared to the lower La/Sm_n samples. A possible explanation for the La/Sm_n pattern is that, except for Pico, the Northeast Seamount lavas came from a common depleted mantle and the elevated La/Sm_n for the Sunray and Fitzroy lavas are from smaller degrees of partial melting.

Ratios of Sm/Yb_n can be used as a measurement of depth of melting (and lithospheric thickness) by taking advantage of the heavy REE being compatible in garnet, and so deeper melting in the garnet stability field of the mantle will increase the Sm/Yb_n ratio (Gibson and Geist, 2010). If lithospheric thickness controls Sm/Yb_n ratios, then we would expect the highest values closest to the thick lithosphere of the Galápagos Platform and decrease to the northeast toward thinner and younger lithosphere (Figure 6). Specifically, we would expect highest Sm/Yb_n at Pico followed by Grande, Sunray, and Fitzroy, then lowest values from Largo, Beagle, and Iguana. Pico does have the highest ratio of 2.2 and the other Northeast Seamount lavas have Sm/Yb_n within a range of 0.9-1.4. The lowest Sm/Yb_n values of 0.8-0.9 are from the western end of Largo (DR72) but the other samples from this seamount have higher ratios (~1.2) comparable to the others. Overall, there is no discernible spatial pattern of Sm/Yb_n and it can vary within individual seamounts, so with the exception Pico, the lithospheric thickness may not be appreciably different in the region of the other seamounts in this study. In fact, the gravity-based model of Feighner and Richards (1994) does not show any data beyond the 8 km line on which Grande, Sunray, and Fitzroy are near.

5.3 Subsidence, Drowned Islands and Paleogeography

The flat tops of several of the seamounts suggest they may be guyots (drowned islands) but by itself a flat top does not necessarily indicate past subaerial erosion, as this feature is evident in other Pacific seamounts by sedimentation and filling of surface topography (e.g, Karig et al., 1970). Another possibility is that the flat top is constructional and not erosional – such mechanisms that have been invoked include lava ponding within a caldera and inflation by shallow lava injection (e.g., Chaytor et al., 2007; Clague et al., 2000; Fornari et al., 1984). Other lines of evidence are used to determine subaerial erosion such as wave cut terraces, oxidized soil layers and terrestrial/tidal sediments (Buchs et al., 2018). Christie et al. (1992) reported the recovery of rounded cobbles on Fitzroy and two orange, weathered basalt cobbles from dredge

PL2-13 near the peak on the eastern end of Largo, leading them to conclude that both had been subaerial. Unfortunately, the existing bathymetric mapping does not have high enough resolution to distinguish wave cut terraces or beaches and the sample dredging was not designed to recover sediments or have any stratigraphic control. Therefore, we rely on subsidence modeling using the radiometric ages and accepted subsidence rates for oceanic lithosphere to calculate which seamounts were subaerial in the past, i.e., were islands, and estimate their age of submergence.

To model the subsidence, we assume that thermal cooling begins after magmatism has ceased so we use the youngest radiometric age for each seamount as the starting point. In order to calculate the range of subsidence from that age, we apply two different rates: 1) that of ridge-derived oceanic lithosphere $d(t) = 365t^{1/2}$ where t is time in millions of years and d is meters of subsidence at time t (Stein and Stein, 1992); and 2) that of the Galápagos Platform (Geist et al., 2014) using $z = -1.14*(age^{1/2}) + 933$ where z is meters of subsidence and age is years. We then subtract the current seamount peak depth from the total subsidence to estimate the initial elevation of the peak of each volcano (Table 5). The calculated subsidence is greatest using the faster platform subsidence rate compared to the ocean lithosphere rate. As a result, the initial island peak elevation is highest using the platform subsidence model and lowest with the oceanic lithosphere model.

The results show that Sunray, Fitzroy, Grande, and Pico were islands in the past, consistent with their flat tops that could have formed by wave erosion. The oceanic lithosphere subsidence rate shows that Sunray, Fitzroy, and Grande were between 300-400 meters above sea level (masl) while the platform rate shows 400-900 masl. The calculated elevations appear to be reasonable considering that the historically active off-platform islands of Pinta and Marchena are currently ~600 and ~200 masl, respectively. The calculated initial elevation for Pico Seamount using the oceanic lithosphere model is 32 masl so it would have been a small, ~ 2 km diameter island – about the same size as Rábida Island located south of Santiago. The platform subsidence-based model shows that Pico would have been 870 masl, which seems unrealistically high considering that Rabida is 250 masl. Beagle and Iguana Seamounts, which do not display the flat top of a guyot, could not have been subaerial as our calculations show that both were never close to the sea surface.

Neither subsidence model shows that the 1.3 Ma age of a pillow basalt from the eastern peak of Largo is enough time for the seamount peak to subside to its current 650 mbsl. If the peak of Largo was at some point subaerial it would need to be older than 2 Ma (using the platform subsidence rate) to 3.2 Ma (using the oceanic lithosphere subsidence rate). The other possibility is that the weathering of the recovered rocks was due to submarine alteration processes (palagonitization) and that Largo was never above sealevel.

The submergence age of the former islands can be estimated using the two subsidence rates and the calculated peak elevations (Table 5). The lifetime of Pico Island could have been as short as 0.3 m.y. using the oceanic lithosphere model or as long as 2.6 m.y. with the platform model, but since we consider the platform model unrealistic for Pico, the former value may be closer to the actual timespan. Sunray and Grande were both islands for approximately the same period, from 3.1-3.3 Ma to 2.2-1 Ma. Fitzroy was emergent at 1.7 Ma and submerged between 0.8-0.3 Ma. The three younger and larger seamounts represent a group of three islands of 5-10 km diameter (based on the proportions of their flat peaks) that existed north of the main Galápagos platform during the period of approximately 3 to 0.5 Ma.

We can reconstruct the paleogeography of the islands and seamounts over the past 5 m.y. using our subsidence calculations and the motion of the Nazca Plate relative to the hotspot reference frame (Figure 7). This replaces a similar model that was presented by Sinton et al. (2014) who used the older and now discarded radiometric ages and did not include data from Largo, Grande and Iguana. We assume that the Nazca Plate has maintained an eastward motion relative to the hotspot at a rate of 39 km-my^{-1} since 5 Ma (Sinton et al., 1996) – this velocity is based on the oldest radiometric ages from the islands. This value lies between the 31 km-my^{-1} present day absolute plate motion velocity model GSRM-APM-1 based on shear wave splitting (Kreemer, 2009) and the NNR-MORVEL56 no-net-rotation model value of 56 km-my^{-1} (Argus et al., 2011). In our model, we overlay the estimated position of the GSC at different time periods (Mittelstaedt et al., 2012; Wilson and Hey, 1995). Pico is the first to erupt on the shallower northern edge of the platform at about 5 Ma (Figure 7) when the GSC was close to or over the hotspot. At 3.8 Ma, Sunray Island is active to the northeast of the main platform where San Cristobal may have been active, although there are no radiometric ages older than 2.3 Ma (White et al., 1993). During the time that Sunray was an active island, Grande Island erupts by 3.1 Ma

to the east of Pico. Between 2.5 Ma and 1.7 Ma, Fitzroy Island and Beagle Seamount were active. Fitzroy would have remained an island for possibly a span of ~ 2 m.y. until 0.8 Ma to 0.3 Ma. Largo Seamount was active at least by 1.3 Ma, which would place it just south of the current position of Genovesa Island. Iguana Seamount (DR83) was the most recent to erupt and the furthest to the east.

In summary, our calculations based on the data presented here indicate that Sunray, Fitzroy, Grande and likely Pico are drowned islands. The existence of drowned Galápagos Islands (Christie et al., 1992; Sinton et al., 2017; Werner et al., 1999) extends the time available for species evolution and inter-island radiation (Benavides et al., 2009; Grant et al., 1996; Parent et al., 2008). The islands of Sunray, Fitzroy, and Grande represent a significant cluster of islands that existed for ~3 m.y. and this will add to the ongoing study of genetic evolution on the archipelago.

5.4 Evolution of Volcano Morphology

There is a change in volcano morphology at ~ 1.5 Ma from the generally conical shapes of Pico, Sunray, Fitzroy, Beagle, and Grande to the east-west elongated, composite morphology of Largo and Iguana (Figure 1). The east-west elongation is also a characteristic of the younger Genovesa Ridge to the west (Harpp et al., 2003, p. 2003). Elongation of seamounts and volcanic lineaments in the NGVP has been attributed to the lithospheric stress field associated with the Galápagos Transform Fault (GTF) (Harpp and Geist, 2002; Harpp et al., 2003) and the extension of the southern part of the GTF at ~ 1 Ma (Mittelstaedt et al., 2012). Linear and conical seamounts are found in other hotspot settings. For example, (Chaytor et al., 2007) observed that the Cobb and Bowie seamounts in the Gulf of Alaska are both conical and linear and suggested that the latter are constructed by eruptions along a pre-existing lithospheric weakness such as fossil transform fault or ridge segment and that subsequent magmatism may eventually focus to a central location and the seamount evolved to a conical shape. Both linear and conical seamounts have been observed in the region of the Azores (Lourenço et al., 1998) with the linear volcanoes attributed to the regional stress field (Casalbore et al., 2015).

The pre-existing structure of the lithosphere below the Northeast Seamounts is not well constrained. However, if we assume that it formed at an E-W trending GSC, we would expect E-W parallel zones of weakness from normal faulting and ridge propagation. The cone shape of the

older volcanoes suggests that there was either no influence from pre-existing structural weakness in the lithosphere and/or there was no dominant direction of regional lithospheric stress. Largo is the closest of the seamounts to the GSC and very likely erupted over the youngest lithosphere (Figure 6) which is estimated to have an age of 3-4 Ma (Villagómez et al., 2011) so its E-W strike could reflect reactivation of normal faulting parallel to the GSC. However, this does not necessarily explain the linearity of Iguana which is the farthest from the ridge axis and presumably erupted on older lithosphere.

5.5 Apparent Eastward Progression of Magmatism

To determine if there is any temporal-spatial pattern of magmatism of the Northeast Seamounts, we plot the oldest age of each seamount versus the longitude of the current location (Figure 8A). In this figure, a line represents the expected age progression of volcanoes that erupted at the current position of the hotspot under Fernandina (91.5°W) assuming that the Nazca plate has been moving eastward at a velocity of 39 km-my^{-1} (Sinton et al., 1996). As we established earlier in this paper, Pico formed over the hotspot so it lies on this trend but all the other seamounts lie well below this line indicating that they erupted east of the current hotspot. There appears to be no pattern to the age and position of these volcanoes in Figure 8A. However, if the longitude of initial magmatism for each seamount is backtracked to the west (Figure 8B), then a pattern does appear. It shows an eastward progression of the location of initial volcanism for all the Northeast seamounts except Pico, which is opposite the general trend for the Galápagos Islands. A simple linear regression of the trend (excluding Pico) is 0.429° longitude-my^{-1} which at this latitude is the equivalent of 47 km-my^{-1}, slightly faster than the velocity of the Nazca plate that we use but within the range of other models. Thus, the location of seamount volcanism seems to be related to plate movement.

One observation that could explain this trend is that the Northeast Seamounts are located at the transitional edge between the thickened (and likely relatively warm) lithosphere of the Galápagos Platform and the thinner, colder surrounding lithosphere (Figure 6). As the platform with its thicker keel moves eastward, some of the asthenosphere displaced by the platform keel could deflected upward and result in decompression melting. This mechanism is based on the concept of shear-driven upwelling (SDU) (Conrad et al., 2010) that has been used to explain non-plume intraplate magmatism such as the Pukapuka, Sojourn, and Hotu-Matua volcanic ridges off the

East Pacific Rise (Ballmer et al., 2013). In these examples, upwelling of the asthenosphere and decompression melting are triggered by horizontal asthenospheric flow in the presence of mantle viscosity heterogeneities caused by pockets of geochemically enriched mantle. Mantle viscosity heterogeneities that trigger SDU can be differences in mantle temperature, composition, or both (Conrad et al., 2011, 2010). If we apply this concept to the Northeast Seamounts, we propose that Pico formed by magmatism associated with the Galápagos mantle plume. When it erupted it was close to the estimated location of the plume center and its composition is consistent with derivation from the CGD/PLUME mantle source (Figures 3 and 7). As the platform migrated eastward, SDU along the platform edge could have been triggered by viscosity differences between the cooler depleted upper mantle and warmer mantle beneath the platform derived from the mantle plume. The slightly incompatible element-enriched lavas from Sunray and Fitzroy indicate that there may have been viscosity differences from geochemically enriched material. In summary, a combination of higher temperature and geochemical enrichment could have provided a viscosity gradient at the boundary between the thick lithosphere of the platform and the thinner lithosphere to the northeast. As this boundary moved eastward with the Nazca plate, it progressively triggered SDU and the creation of the Northeast seamounts and islands.

7 Acknowledgements

The work presented here was supported by the US National Science Foundation (grants OCE-89-11826 and OC-1157461) and by the German Ministry for Education and Research (BMBF; grant 03G0158A). We would like to thank the NSF-supported (OCE-1558679) core repository at Oregon State University for access to the archived PLUME2 samples. We thank Anthony Koppers, Bob Duncan, and Sidney Hemming for assistance with the radiometric dating. We appreciate the helpful reviews from Iain Neill, David Buchs, and Andrew Kerr.

References

Argus, D.F., Gordon, R.G., DeMets, C., 2011. Geologically current motion of 56 plates relative to the no-net-rotation reference frame. Geochemistry, Geophysics, Geosystems 12.

Ballmer, M.D., Conrad, C.P., Smith, E.I., Harmon, N., 2013. Non-hotspot volcano chains produced by migration of shear-driven upwelling toward the East Pacific Rise. Geology 41, 479–482.

Benavides, E., Baum, R., Snell, H.M., Snell, H.L., Sites, J., Jack W., 2009. Island Biogeography of Galápagos Lava Lizards (tropiduridae: Microlophus): Species Diversity and Colonization of the Archipelago. Evolution 63, 1606–1626.

Byrnes, J.S., Hooft, E.E.E., Toomey, D.R., Villagómez, D.R., Geist, D.J., Solomon, S.C., 2015. An upper mantle seismic discontinuity beneath the Galápagos Archipelago and its implications for studies of the lithosphere-asthenosphere boundary. Geochemistry, Geophysics, Geosystems 16, 1070–1088.

Buchs, D.M., Williams, R., Sano, S., Wright, V.P., 2018. Non-Hawaiian lithostratigraphy of Louisville seamounts and the formation of high-latitude oceanic islands and guyots. Journal of Volcanology and Geothermal Research.

Casalbore, D., Romagnoli, C., Pimentel, A., Quartau, R., Casas, D., Ercilla, G., Hipólito, A., Sposato, A., Chiocci, F.L., 2015. Volcanic, tectonic and mass-wasting processes offshore Terceira Island (Azores) revealed by high-resolution seafloor mapping. Bulletin of Volcanology 77, 24.

Chaytor, J.D., Keller, R.A., Duncan, R.A., Dziak, R.P., 2007. Seamount morphology in the Bowie and Cobb hot spot trails, Gulf of Alaska. Geochemistry, Geophysics, Geosystems 8. https://doi.org/10.1029/2007GC001712

Christie, D.M., Duncan, R.A., McBirney, A.R., Richards, M.A., White, W.M., Harpp, K.S., Fox, C.G., 1992. Drowned islands downstream from the Galápagos hotspot imply extended speciation times. Nature 355, 246–248.

Conrad, C.P., Bianco, T.A., Smith, E.I., Wessel, P., 2011. Patterns of intraplate volcanism controlled by asthenospheric shear. Nature Geoscience 4, 317. https://doi.org/10.1038/ngeo1111

Conrad, C.P., Wu, B., Smith, E.I., Bianco, T.A., Tibbetts, A., 2010. Shear-driven upwelling induced by lateral viscosity variations and asthenospheric shear: A mechanism for intraplate volcanism. Physics of the Earth and Planetary Interiors 178, 162–175.

Duncan, R.A., Hogan, L.G., 1994. Radiometric dating of young MORB using the 40Ar-39Ar incremental heating method. Geophysical Research Letters 21, 1927–1930.

Feighner, M.A., Richards, M.A., 1994. Lithospheric structure and compensation mechanisms of the Galápagos Archipelago. Journal of Geophysical Research 99, 6711–6729.

Garbe-Schönberg, C., 1993. Simultaneous determination of thirty-seven trace elements in twenty-eight international rock standards by ICP-MS. Geostandards and Geoanalytical Research 17, 81–97.

Geist, D.J., McBirney, A.R., Duncan, R.A., 1986. Geology and petrogenesis of lavas from San Cristobal Island, Galápagos Archipelago. Geological Society of America Bulletin 97, 555–566.

Geist, D.J., Naumann, T.R., Standish, J.J., Kurz, M.D., Harpp, K.S., White, W.M., Fornari, D.J., 2005. Wolf Volcano, Galápagos Archipelago: Melting and magmatic evolution at the margins of a mantle plume. Journal of Petrology 46, 2197–2224.

Geist, D.J., Snell, H., Snell, H., Goddard, C., Kurz, M.D., 2014. A Paleogeographic Model of the Galápagos Islands and Biogeographical and Evolutionary Implications, in: Harpp, K.S., Mittelstaedt, E., d'Ozouville, N., Graham, D.W. (Eds.), The Galápagos: A Natural Laboratory for the Earth Sciences. John Wiley & Sons, Inc, pp. 145-166.

Geldmacher, J., Hanan, B.B., Blichert-Toft, J., Harpp, K., Hoernle, K., Hauff, F., Werner, R., Kerr, A.C., 2003. Hafnium isotopic variations in volcanic rocks from the Caribbean

Large Igneous Province and Galápagos hot spot tracks. Geochemistry, Geophysics, Geosystems 4, 1062, doi:10.1029/2002GC000477, 7.

Gibson, S.A., Geist, D., 2010. Geochemical and geophysical estimates of lithospheric thickness variation beneath Galápagos. Earth and Planetary Science Letters 300, 275–286. https://doi.org/10.1016/j.epsl.2010.10.002

Govindaraju, K., 1994. 1994 compilation of working values and sample description for 383 geostandards. Geostandards and Geoanalytical Research 18, 1–158.

Graham, D.W., Christie, D.M., Harpp, K.S., Lupton, J.E., 1993. Mantle plume helium in submarine basalts from the Galápagos Platform. Science 262, 2023–2026.

Graham, D.W., Hanan, B.B., Lupton, J.E., Hoernle, K., Werner, R., Christie, D.M., Sinton, J.M., 2014. Helium isotope variations and mantle plume-spreading ridge interactions along the Galápagos Spreading Center. in: Harpp, K.S., Mittelstaedt, E., d'Ozouville, N., Graham, D.W. (Eds.), The Galápagos: A Natural Laboratory for the Earth Sciences. John Wiley & Sons, Inc, pp. 393–414.

Grant, P.R., Grant, B.R., Deutsch, J.C., 1996. Speciation and hybridization in island birds [and Discussion]. Philosophical Transactions of the Royal Society of London B: Biological Sciences 351, 765–772.

Harpp, K., Geist, D., 2002. Wolf–Darwin lineament and plume–ridge interaction in northern Galápagos. Geochemistry, Geophysics, Geosystems 3.

Harpp, K.S., Fornari, D.J., Geist, D.J., Kurz, M.D., 2003. Genovesa Submarine Ridge: A manifestation of plume-ridge interaction in the northern Galápagos Islands. Geochemistry, Geophysics, Geosystems 4.

Harpp, K.S., White, W.M., 2001. Tracing a mantle plume: Isotopic and trace element variations of Galápagos seamounts. Geochemistry, Geophysics, Geosystems 2.

Harpp, K.S., Wirth, K.R., Korich, D.J., 2002. Northern Galápagos Province: Hotspot-induced, near-ridge volcanism at Genovesa Island. Geology 30, 399–402.

Harpp, K.S., Wirth, K.R., Teasdale, R., Blair, S., Reed, L., Barr, J., Pistiner, J., Korich, D., 2014. Plume-ridge interaction in the Galápagos: Perspectives from Wolf, Darwin and Genovesa Islands. in: Harpp, K.S., Mittelstaedt, E., d'Ozouville, N., Graham, D.W. (Eds.), The Galápagos: A Natural Laboratory for the Earth Sciences. John Wiley & Sons, Inc, pp. 285–334.

Hoernle, K., Abt, D.L., Fischer, K.M., Nichols, H., Hauff, F., Abers, G.A., van den Bogaard, P., Heydolph, K., Alvarado, G., Protti, M., Strauch, W., 2008. Arc-parallel flow in the mantle wedge beneath Costa Rica and Nicaragua. Nature 451, 1094–1097.

Hoernle, K., Hauff, F., Kokfelt, T.F., Haase, K., Garbe-Schönberg, D., Werner, R., 2011. On- and off-axis chemical heterogeneities along the South Atlantic Mid-Ocean-Ridge (5–11°S): Shallow or deep recycling of ocean crust and/or intraplate volcanism? Earth and Planetary Science Letters 306, 86–97.

Hoernle, K., Werner, R., Morgan, J.P., Garbe-Schönberg, D., Bryce, J., Mrazek, J., 2000. Existence of complex spatial zonation in the Galápagos plume. Geology 28, 435–438.

Hooft, E.E.E., Toomey, D.R., Solomon, S.C., 2003. Anomalously thin transition zone beneath the Galápagos hotspot. Earth and Planetary Science Letters 216, 55–64.

Jochum, K.P., Weis, U., Schwager, B., Stoll, B., Wilson, S.A., Haug, G.H., Andreae, M.O., Enzweiler, J., 2016. Reference values following ISO guidelines for frequently requested rock reference materials. Geostandards and Geoanalytical Research 40, 333–350.

Karig, D.E., Peterson, M.N.A., Short, G.G., 1970. Sediment-capped guyots in the Mid-Pacific mountains. Deep Sea Research and Oceanographic Abstracts 17, 373–378. https://doi.org/10.1016/0011-7471(70)90029-X

Koppers, A.A.P., 2002. ArArCALC—software for $^{40}Ar/^{39}Ar$ age calculations. Computers & Geosciences 28, 605–619.

Koppers, A.A.P., Russell, J.A., Roberts, J., Jackson, M.G., Konter, J.G., Wright, D.J., Staudigel, H., Hart, S.R., 2011. Age systematics of two young en echelon Samoan volcanic trails. Geochemistry, Geophysics, Geosystems 12.

Kreemer, C., 2009. Absolute plate motions constrained by shear wave splitting orientations with implications for hot spot motions and mantle flow. Journal of Geophysical Research 114.

Kurz, M.D., Geist, D., 1999. Dynamics of the Galápagos hotspot from helium isotope geochemistry. Geochimica et Cosmochimica Acta 63, 4139–4156.

Lanphere, M.A., Dalrymple, B., 1976. Identification of excess 40Ar by the $^{40}Ar/^{39}Ar$ age spectrum technique. Earth and Planetary Science Letters 32, 141–148.

Lourenço, N., Miranda, J.M., Luis, J.F., Ribeiro, A., Victor, L.A.M., Madeira, J., Needham, H.D., 1998. Morpho-tectonic analysis of the Azores Volcanic Plateau from a new bathymetric compilation of the area. Marine Geophysical Researches 20, 141–156.

Min, K., Mundil, R., Renne, P.R., Ludwig, K.R., 2000. A test for systematic errors in $^{40}Ar/^{39}Ar$ geochronology through comparison with U/Pb analysis of a 1.1-Ga rhyolite. Geochimica et Cosmochimica Acta 64, 73–98.

Mittal, T., Richards, M.A., 2017. Plume-ridge interaction via melt channelization at Galápagos and other near-ridge hotspot provinces. Geochemistry, Geophysics, Geosystems 18.

Mittelstaedt, E., Ito, G., 2005. Plume-ridge interaction, lithospheric stresses, and the origin of near-ridge volcanic lineaments. Geochemistry, Geophysics, Geosystems 6.

Mittelstaedt, E., Soule, A.S., Harpp, K.S., Fornari, D.J., 2014. Variations in crustal thickness, plate rigidity, and volcanic processes throughout the Northern Galápagos Volcanic Province, in: Harpp, K.S., Mittelstaedt, E., d'Ozouville, N., Graham, D.W. (Eds.), The Galápagos: A Natural Laboratory for the Earth Sciences. John Wiley & Sons, Inc, pp. 263-284

Mittelstaedt, E., Soule, S., Harpp, K., Fornari, D., McKee, C., Tivey, M., Geist, D., Kurz, M.D., Sinton, C., Mello, C., 2012. Multiple expressions of plume-ridge interaction in the Galápagos: Volcanic lineaments and ridge jumps. Geochemistry, Geophysics, Geosystems 13.

Morgan, W.J., 1978. Rodriguez, Darwin, Amsterdam, ..., A Second Type of Hotspot Island. Journal of Geophysical Research 83, 5,355-5,360.

Morgan, W.J., 1972. Deep mantle convection plumes and plate motions. AAPG Bulletin 56, 203–213.

Parent, C.E., Caccone, A., Petren, K., 2008. Colonization and diversification of Galápagos terrestrial fauna: a phylogenetic and biogeographical synthesis. Philosophical Transactions of the Royal Society B: Biological Sciences 363, 3347–3361.

Peterson, M.E., Saal, A.E., Kurz, M.D., Hauri, E.H., Blusztajn, J.S., Harpp, K.S., Werner, R., Geist, D.J., 2017. Submarine basaltic glasses from the Galápagos Archipelago: determining the volatile budget of the mantle plume. Journal of Petrology 58, 1419–1450.

Pringle, M.S., 1993. Age progressive volcanism in the Musicians Seamounts: A test of the hot spot hypothesis for the Late Cretaceous Pacific, in: Pringle, M.S., Sager, W.W., Sliter,

W.V., Stein, S. (Eds.), Geophysical Monograph Series. American Geophysical Union, Washington, D. C., pp. 187–215.

Renne, P.R., Swisher, C.C., Deino, A.L., Karner, D.B., Owens, T.L., DePaolo, D.J., 1998. Intercalibration of standards, absolute ages and uncertainties in $^{40}Ar/^{39}Ar$ dating. Chemical Geology 145, 117–152.

Roddick, J.C., 1978. The application of isochron diagrams in ^{40}Ar-^{39}Ar dating: A discussion. Earth and Planetary Science Letters 41, 233–244.

Ryan, W.B.F., Carbotte, S.M., Coplan, J.O., O'Hara, S., Melkonian, A., Arko, R., Weissel, R.A., Ferrini, V., Goodwillie, A., Nitsche, F., Bonczkowski, J., Zemsky, R., 2009. Global Multi-Resolution Topography synthesis. Geochemistry Geophysics Geosystems 10.

Saal, A.E., Kurz, M.D., Hart, S.R., Blusztajn, J.S., Blichert-Toft, J., Liang, Y., Geist, D.J., 2007. The role of lithospheric gabbros on the composition of Galápagos lavas. Earth and Planetary Science Letters 257, 391–406. https://doi.org/10.1016/j.epsl.2007.02.040

Schilling, J.-G., Fontignie, D., Blichert-Toft, J., Kingsley, R., Tomza, U., 2003. Pb-Hf-Nd-Sr isotope variations along the Galápagos Spreading Center (101°–83°W): Constraints on the dispersal of the Galápagos mantle plume. Geochemistry, Geophysics, Geosystems 4.

Sharp, W.D., Renne, P.R., 2005. The $^{40}Ar/^{39}Ar$ dating of core recovered by the Hawaii Scientific Drilling Project (phase 2), Hilo, Hawaii. Geochemistry, Geophysics, Geosystems 6.

Sinton, C.W., 1992. The evolution of the Galápagos Platform: results from radiometric dating and experimental petrology (Thesis/Dissertation). Oregon State University.

Sinton, C.W., Christie, D.M., Coombs, V.L., Nielsen, R.L., Fisk, M.R., 1993. Near-primary melt inclusions in anorthite phenocrysts from the Galápagos Platform. Earth and Planetary Science Letters 119, 527–537.

Sinton, C.W., Christie, D.M., Duncan, R.A., 1996. Geochronology of Galápagos seamounts. Journal of Geophysical Research 101, 13,689-13,700.

Sinton, C.W., Harpp, K.S., Christie, D.M., 2014. A Preliminary Survey of the Northeast Seamounts, Galápagos Platform, in: Harpp, K.S., Mittelstaedt, E., d'Ozouville, N., Graham, D.W. (Eds.), The Galápagos. John Wiley & Sons, pp. 335–362.

Sinton, C.W., Harpp, K.S., Geist, D.J., Mittelstaedt, E., Fornari, D.J., Soule, S.A., 2017. Banco Tuzo: an ancient Galápagos island and potential stepping stone for species dispersal. Galápagos Research 69.

Sinton, J., Detrick, R., Canales, J.P., Ito, G., Behn, M., 2003. Morphology and segmentation of the western Galápagos Spreading Center, 90.5°–98°W: Plume-ridge interaction at an intermediate spreading ridge. Geochemistry, Geophysics, Geosystems 4,

Stein, C.A., Stein, S., 1992. A model for the global variation in oceanic depth and heat flow with lithospheric age. Nature 359, 123–129. https://doi.org/10.1038/359123a0

Sun, S.–., McDonough, W.F., 1989. Chemical and isotopic systematics of oceanic basalts: implications for mantle composition and processes. Geological Society, London, Special Publications 42, 313–345.

Taylor, J.R., 1997. An introduction to error analysis: the study of uncertainties in physical measurements. University Science Books, New York.

Villagómez, D.R., Toomey, D.R., Geist, D.J., Hooft, E.E., Solomon, S.C., 2014. Mantle flow and multistage melting beneath the Galápagos hotspot revealed by seismic imaging. Nature Geoscience 7, 151–156.

Villagómez, D.R., Toomey, D.R., Hooft, E.E., Solomon, S.C., 2011. Crustal structure beneath the Galápagos Archipelago from ambient noise tomography and its implications for plume-lithosphere interactions. Journal of Geophysical Research: Solid Earth 116.

Werner, R., Hoernle, K., Barckhausen, U., Hauff, F., 2003. Geodynamic evolution of the Galápagos hot spot system (Central East Pacific) over the past 20 m.y.: Constraints from morphology, geochemistry, and magnetic anomalies. Geochemistry, Geophysics, Geosystems 4.

Werner, R., Hoernle, K., van den Bogaard, P., Ranero, C., von Huene, R., Korich, D., 1999. Drowned 14-m.y.-old Galápagos archipelago off the coast of Costa Rica: Implications for tectonic and evolutionary models. Geology 27, 499–502.

White, W.M., McBirney, A.R., Duncan, R.A., 1993. Petrology and Geochemistry of the Galápagos Islands: portrait of a pathological mantle plume. Journal of Geophysical Research: Solid Earth 98, 19,533-19,563

Wilson, D.S., Hey, R.N., 1995. History of rift propagation and magnetization intensity for the Cocos-Nazca spreading center. Journal of Geophysical Research 100, 10,041-10,056.

York, D., 1968. Least squares fitting of a straight line with correlated errors. Earth and Planetary Science Letters 5, 320–324.

Figure Captions

Figure 1. Map of the Galápagos region – the red rectangle shows the extent of the map of the Northeast Seamounts, the dashed white line marks the NGVP. Contour line interval is 400 m. Dredge sites are shown with white circles. The maps were made using bathymetry from GeoMapApp (Ryan et al., 2009).

Figure 2. Primitive mantle-normalized trace element diagrams for examples of **A** depleted and **B** enriched lavas of the Northeast Seamounts presented in this paper and from Sinton et al. (2014). Normalizing values are from Sun and McDonough (1989).

Figure 3. Plots of $^{87}Sr/^{86}Sr$ vs. εNd and $^{206}Pb/^{204}Pb$ vs. $^{208}Pb/^{204}Pb$ for the Northeast Seamounts. Data are from Table 2 and some PLUME2 (PL) samples are from Harpp and White (2001). Blue circles represent samples with depleted incompatible trace elements, black circles are samples with moderate trace element enrichment from Sunray and Fitzroy (Figure 2), and the red circle is the sample from Pico (PL2-16). The one sample from Pico (PL2-16-3) does not have reported $^{87}Sr/^{86}Sr$ so the red line represents the εNd value for that sample. The Eastern Galápagos Spreading Center (EGSC) field is composed of data from samples recovered east of the 90.5°W transform and west of the 85°W transform (Graham et al., 2014; Schilling et al., 2003). The Genovesa field represents data from (Harpp et al., 2014) and White et al. (1993). Stars represent the end members for the four mantle sources described by Harpp and White (2001). Overlain are fields for the Eastern Galápagos Domain (EGD), Central Galápagos Domain (CGD), Northern Galápagos Domain (NGD), and Southern Galápagos Domain (SGD) (Geldmacher et al., 2003; Hoernle et al., 2000; Werner et al., 2003).

Figure 4. Incremental heating $^{40}Ar/^{39}Ar$ age spectra for Galápagos Northeast Seamount basalts. The $^{40}Ar/^{39}Ar$ "plateau" ages are weighted with errors reported at the 95% confidence level, including 0.3–0.5% standard deviations in the J-value. All ages were calculated based on the flux monitor FCT-3 biotite age of 28.03 ± 0.18 Ma (Renne et al., 1998). These data and isochron ages are presented in Table 3.

Figure 5. Chondrite normalised La/Sm and Sm/Yb ratios from data presented here and from Sinton et al. (2014). Blue circles represent samples with depleted incompatible trace elements, black circles are samples with moderate trace element enrichment from Sunray and Fitzroy

(Figure 2), and the red circle is the sample from Pico (PL2-16). Chondrite values are from Sun and McDonough (1989). Lower degrees of partial melting in the spinel lherzolite stability area of the shallow mantle will result an increase in La/Sm_n but have little effect on Sm/Yb_n. Lower degrees of partial melting at greater depths where garnet is stable will result in an increase in both La/Sm_n and Sm/Yb_n.

Figure 6. Schematic map showing the modeled crustal thickness (km) based on gravity measurements (Feighner and Richards, 1994) and modeled crustal ages based on interpretations of magnetic anomalies and plate reconstructions are shown in the colored lines (Villagómez et al., 2011).

Figure 7. Paleoreconstruction of the Northeast Seamounts and Galápagos Islands from 5 Ma to present. The positions of the islands are based on paleoreconstructions from Geist et al (2014). The paleopositions of the GSC are based on Mittelstaedt et al. (2012) for the area west of the hotspot and Wilson and Hey (1995) for the area east of the hotspot. The locations of the seamounts are based on an eastward motion the Nazca plate at 39 km/m.y (Sinton et al., 1996). Active volcanism is noted with the volcano icon with ash plume and an emergent island has a horizontal sea-level line. Banco Tuzo is a large, flat-topped seamount south of Marchena that appears to have been an island at 1-2 Ma (Sinton et al., 2017). Overlain are fields for the Eastern Galápagos Domain (EGD), Central Galápagos Domain (CGD), Northern Galápagos Domain (NGD), and Southern Galápagos Domain (SGD) (Geldmacher et al., 2003; Hoernle et al., 2000; Werner et al., 2003). Note that Pico formed in the central Galápagos domain consistent with its enriched incompatible element and isotopic composition (see Figures 2 and 3). Both Sunray and Grande remain islands until sometime between 1-2 Ma, depending on the subsidence model used.

Figure 8. A: Plot of oldest age for each seamount and longitude of the current position. The dashed line is the eastward plate motion of the Nazca plate at 39 km/m.y. relative to the hotspot (Sinton et al., 1996) assuming zero age is at Fernandina (91.5°W). Abbreviated seamount names are: PC - Pico; SN - Sunray; GR - Grande; FZ - Fitzroy; BG - Beagle; LG – Largo; IG – Iguana. **B:** Plot of oldest age for each seamount and the calculated longitude of initial eruption using 39 km/m.y.

Table 1. Dredge Locations and Sample Descriptions for the Northeast Seamounts

Seamount/ Dredge #	Dredge Location[1]	Dredge Depth[2] (m)	Sample Descriptions[3]
Sunray			
PL2-9	00° 28.13'S 88° 32.11'W	1425-935	Three lava groups: 9A (sample 9-50 and -56) high to moderately vesicular, aphyric, La_n/Sm_n 1.0-1.3; 9B moderately vesicular, aphyric with higher MgO than 9A, La_n/Sm_n 1.0-1.3; 9C non-vesicular with sparse plagioclase, spinel, and olivine microphenocrysts with spinel inclusions, La_n/Sm_n 0.33.
PL2-10	00° 34.04'S 88° 35.44'W	1141-1006	Two lava groups: 10A weathered, slightly vesicular basalts with small olivine phenocrysts and abundant (ultraphyric) 1cm embayed plagioclase megacrysts; 10B (sample 10-5) Moderately vesicular; small aggregates of plagioclase and olivine; a few skeletal plagioclase phenocrysts with spinel inclusions, La_n/Sm_n 0.56.
Fitzroy			
PL2-11	00° 11.70'S 88° 40.10'W	1309-702	Two lava groups: 11A (sample 11-7) a non-vesicular basalt with plagioclase megacrysts and olivine microphenocrysts, La_n/Sm_n 0.41; 11B (sample 11-5) highly vesicular, aphyric basalts, La_n/Sm_n 1.0.
PL2-12	00° 14.45'S 88° 38.20'W	1378-1123	Two lava groups: 12A (sample 12-1 and -5) moderately vesicular with plagioclase and olivine phenocrysts, La_n/Sm_n 0.45; 12B (sample 12-7 and remainder) moderately vesicular with plagioclase phenocrysts/megacrysts and small olivine phenocrysts, primitive glass compositions with MgO ~9.5 wt, La_n/Sm_n 0.33.
Beagle			
DR80	00° 01.43' S 88° 30.97' W	1657-1555	Aphyric pillow basalt fragment with some vesicles in the unaltered interior, La_n/Sm_n 0.41.
Largo			
PL2-13	00° 05.80'N 89° 02.90'W	1400-700	Two lava groups: 13A slightly vesicular, plagioclase ultraphyric basalts with primitive glass compositions (MgO ~10 wt.%), La_n/Sm_n 0.24; 13B slightly vesicular, aphyric basalts with occasional olivine and plagioclase phenocrysts, MgO 8-9 wt.%, La_n/Sm_n 0.22-0.29.
PL2-14	00° 06.00'N 89° 05.80'W	1639-1090	Nonvesicular basalts with small spinel phenocrysts and up to 25% olivine, La_n/Sm_n 0.22-0.45.
DR72	00°06.95' N 89°17.40' W	2129-1325	Aphyric pillow basalt fragments with glassy rims, La_n/Sm_n 0.33.
DR72A	00°05.846' N 89°15.006' W	1557-1325	Aphyric pillow basalt fragments with glassy rims, La_n/Sm_n 0.24.
Grande			
DR73	00° 02.82'S 89° 16.26'W	1632-1500	Aphyric, nonvesicular pillow basalt fragment with weathered exterior and fresh interior, La_n/Sm_n 0.40.
Pico			
PL2-16	00° 06.44'S 89° 49.26'W	1688-1320	Three basalt fragments, La_n/Sm_n 1.68.
Iguana			
DR83	00° 18.90'S 88° 23.27' W	1429-1214	Nonvesicular, aphyric basalt fragment with sparse plagioclase phenocrysts, La_n/Sm_n 0.30.

[1]Position on-bottom.
[2]On-bottom to off-bottom depths.
[3]The PL2 dredge descriptions are from Sinton et al. (2014).

Table 2: Major and Trace Element and Radiogenic Isotopic Data

	DR72-1	DR72-3*	DR72a-1	DR73-4	DR80-1	DR83-1	PL2-16-3
SiO_2	47.4	48.71	46.83	47.8	50.18	46.64	46.25
TiO_2	0.80	0.85	0.85	2.02	1.29	0.94	3.07
Al_2O_3	17.12	17.00	18.39	14.31	15.32	17.37	15.53
Fe2O3	10.80	9.87	8.54	13.26	9.68	9.32	14.37
MnO	0.16	0.19	0.13	0.15	0.17	0.14	0.2
MgO	8.70	8.81	9.72	5.35	7.03	8.55	5.14
CaO	11.88	12.23	12.52	11.79	12.9	12.92	11.25
Na_2O	2.47	2.38	2.26	3.27	2.63	2.47	2.9
K_2O	0.05	0.03	0.07	0.15	0.16	0.10	0.34
P_2O_5	0.07	0.04	0.08	0.2	0.14	0.09	0.782
Total	99.45	100.10	99.39	98.30	99.50	98.54	99.85
Sc				54.2	54.5	40.8	32
V				358.3	333.8	233.2	335
Cr				104.0	239.6	305.1	19
Co				45.6	65.0	51.2	68
Ni				49.0	131.4	203.3	29
Cu				77.7	149.6	131.7	69
Zn				103.4	85.6	67.1	
Rb	0.28	0.14	1.17	3.25	2.07	2.03	3.87
Sr	93	84	141	149	112	145	341
Y	22	21	21	45.19	33.58	23.71	44

Zr	39	37	47	129.82	75.34	59.30	178
Nb	0.56	0.76	0.30	1.64	1.21	0.48	22.5
Ba	5.52	3.75	2.85	9.80	8.45	2.10	95
La	0.8	0.9	0.7	2.9	1.9	1.1	16.3
Ce	3.5	3.7	3.7	10.9	6.9	5.2	38.5
Pr	0.7	0.8	0.8	2.2	1.4	1.1	5.0
Nd	4.1	4.7	5.1	12.6	7.7	6.6	23.9
Sm	1.7	1.8	2.0	4.7	2.9	2.4	6.3
Eu	0.7	0.8	0.9	1.8	1.2	1.0	2.1
Gd	2.4	2.8	2.6	6.1	4.0	3.2	7.0
Tb	0.5	0.5	0.5	1.1	0.7	0.6	1.1
Dy	3.3	3.8	3.2	7.1	5.0	4.1	6.9
Ho	0.7	0.8	0.7	1.5	1.0	0.9	1.4
Er	2.0	2.4	1.9	4.0	2.9	2.5	3.7
Tm	0.3	0.4	0.3	0.6	0.4	0.4	0.5
Yb	2.0	2.5	1.9	3.8	2.9	2.5	3.2
Lu	0.3	0.4	0.3	0.6	0.4	0.4	0.5
Hf	1.0	1.3	1.3	3.2	1.9	1.7	4.6
Ta	0.04	0.05	0.03	0.11	0.07	0.05	
Pb	0.15	0.28	0.22	0.54	0.39	0.30	1.51
Th	0.03	0.03	0.02	0.13	0.09	0.04	1.59
U	0.03	0.01	0.33	0.21	0.10	0.09	0.54

*major element analysis is from Peterson et al. (2017)

Table 2 Cont'd

	DR72-1	**DR72-3**	**DR72a-1**	**DR73-4**	**DR80-1**	**DR83-1**	**PL2-9-50**	**PL2-11-7**	**PL 12-05**	**PL2-12-7**	**PL2-13-34**
$^{87}Sr/^{86}Sr$	0.702583	0.702567	0.702526	0.702524	0.702618	0.702539	0.702709	0.702671	0.702574	0.702925	0.702748
$^{143}Nd/^{144}Nd$	0.513110	0.513118	0.513149	0.513144	0.513114	0.513142	0.513076	0.513111	0.513124	0.513135	0.513122
εNd	9.20	9.37	9.97	9.87	9.29	9.83	8.55	9.22	9.47	9.69	9.45
$^{206}Pb/^{204}Pb$	18.655	18.666	18.337	18.374	18.420	18.384	18.6103	18.5212	18.4408	18.3859	18.4838
$^{207}Pb/^{204}Pb$	15.508	15.516	15.495	15.499	15.509	15.500	15.5355	15.5117	15.5085	15.4996	15.5231
$^{208}Pb/^{204}Pb$	38.076	38.112	37.833	37.881	37.961	37.855	38.2176	37.9813	37.9451	37.8711	38.0655

Table 3: Incremental Heating ^{40}Ar-^{39}Ar Analyses for Northeast Seamount Basalts

		Age Spectrum						Total Fusion		Isochron	
Sample	**K_2O[a] (wt.%)**	**Age ± 2σ**	**^{39}Ar %**	**K/Ca[b]**	**MSWD**	**n[c]**	**N[c]**	**Age ± 2σ**	**Age ± 2σ**	**$^{40}Ar/^{36}Ar$ Intercept**	**MSWD**
Sunray											
PL2-9-56	0.32	3.11 ± 0.21	76	0.01	0.5	1	2	3.02 ± 0.01	3.1 ± 3.9	296.3 ± 293.0 ±	0.5
PL2-10-5		3.8 ± 0.1	74	1	1.6	8	18	4.2 ± 0.1	0.3	10.2	1.8
Fitzroy											
PL2-11-5	0.38	1.89 ± 0.05	89	0.043	2.0	16	20	1.86 ± 0.05	1.9 ± 0.1	295.3 ± 5.2	2.1
PL2-11-7	0.19	2.5 ± 0.1	87	0.008	1.5	13	20	2.7 ± 0.1	2.4 ± 0.3	298.7 ± 3.8	1.3
PL2-12-5	0.20	1.7 ± 0.2	100	0.004	1.4	18	18	1.6 ± 0.2	1.9 ± 0.5	293.1 ± 6.1	1.5
Beagle											
DR80-1	0.16	2.2 ± 0.1	100	0.005	1.8	20	20	2.1 ± 0.1	2.6 ± 0.2	291.1 ± 2.1	1.0
Largo											
PL2-13-4	0.11	1.3 ± 0.3	80	0.003	1.5	13	20	1.5 ± 0.2	0.9 ± 0.3	301.7 ± 5.6	1.1
Grande											
DR73-4	0.15	3.3 ± 0.2	85	0.005	2.0	14	20	3.2 ± 0.2	3.4 ± 0.3	293.8 ± 2.7	1.9
Iguana											
DR83-1	0.10	0.5 ± 0.3	74	0.002	0.4	15	20	0.9 ± 0.3	0.6 ± 0.4	294.3 ± 2.7	0.4
Pico											
PL2-16-3a	0.34	5.3 ± 0.5	100	0.24	0.6	8	8	5.0 ± 1.1	5.3 ± 3.4	305.3 ± 10.6	0.2
PL2-16-3b	0.34	5.1 ± 0.5	100	0.12	0.6	11	11	4.8 ± 0.7	5.1 ± 1.5	303.1 ± 6.1	0.2

[a]K_2O data for the PL2 samples are from *Sinton et al.*, [2014] and unpublished for the DR samples.
[b]K/Ca values were calculated as weighted means for the age spectra or as total fusion K/Ca values by combining the gas analyses.
[c]"n" refers to the number of steps included in the age plateau and isochron calculations and "N" is the total number of incremental heating steps for each analysis.
[d]Age recalculated using the initial $^{40}Ar/^{36}Ar$ intercept from the isochron.

Table 4: Comparison of New and Previously Reported ^{40}Ar-^{39}Ar Ages

Seamount	Sample	New Age ± 2σ (Ma)	Old Age ± 2σ (Ma)
Sunray	PL2-9-50	3.1 ± 0.1	5.7 ± 1.2
Sunray	PL2-9-56	3.11 ± 0.07	NA
Sunray	PL2-10-5	3.8 ± 0.1	5.6 ± 0.1
Fitzroy	PL2-11-2 & -5	1.89 ± 0.05	3.2 ± 1.0[1]
Fitzroy	PL2-11-7	2.5 ± 0.1	NA
Fitzroy	PL2-12-5	1.7 ± 0.2	NA
Pico	PL2-16-2 & -3	5.2 ± 0.5[2]	5.6 ± 0.6

[1]Analyses of PL2-11-2 which has similar chemistry to PL2-11-5
[2]Analysis reported here is from sample PL2-16-3

Table 5: Calculation of Subsidence and Initial Elevation of Northeast Seamounts

Seamount	Min. Age (Ma)	Current Peak Depth (m)	Oceanic[1] subsidence (m)	Platform[2] subsidence (m)	Initial Elevation[3] (masl)	Submergence Age (Ma)
Pico	5.2	800	832	1667	32-867	4.9-2.6
Grande	3.3	250	663	1138	413-888	2.2-0.8
Fitzroy	1.7	150	476	553	326-403	0.8-0.3
Beagle	2.2	800	541	758	submerged	NA
Sunray	3.1	370	643	1074	273-704	2.2-1.0
Largo	1.3	650	416	367	submerged	NA
Iguana	0.5	1215	258	127	submerged	NA

[1]The total calculated subsidence using the minimum age and the subsidence rate of oceanic lithosphere from Stein and Stein (1992).

[2]The total calculated subsidence using the minimum age and the subsidence rate of the Galapagos Platform from Geist et al. (2014).

Age Progressive Volcanism Opposite Nazca Plate Motion: Insights from Seamounts and Drowned Islands on the Northeastern Margin of the Galápagos Platform

Highlights

- Four of the seven seamounts northeast of the Galápagos Platform are drowned islands
- The ages of the seamounts range from 5.2 Ma to 0.5 Ma
- Seamount morphology changes from conical to elongate at ~1.5 Ma
- The locus of volcanism appears to migrate eastward at the rate of Nazca plate motion

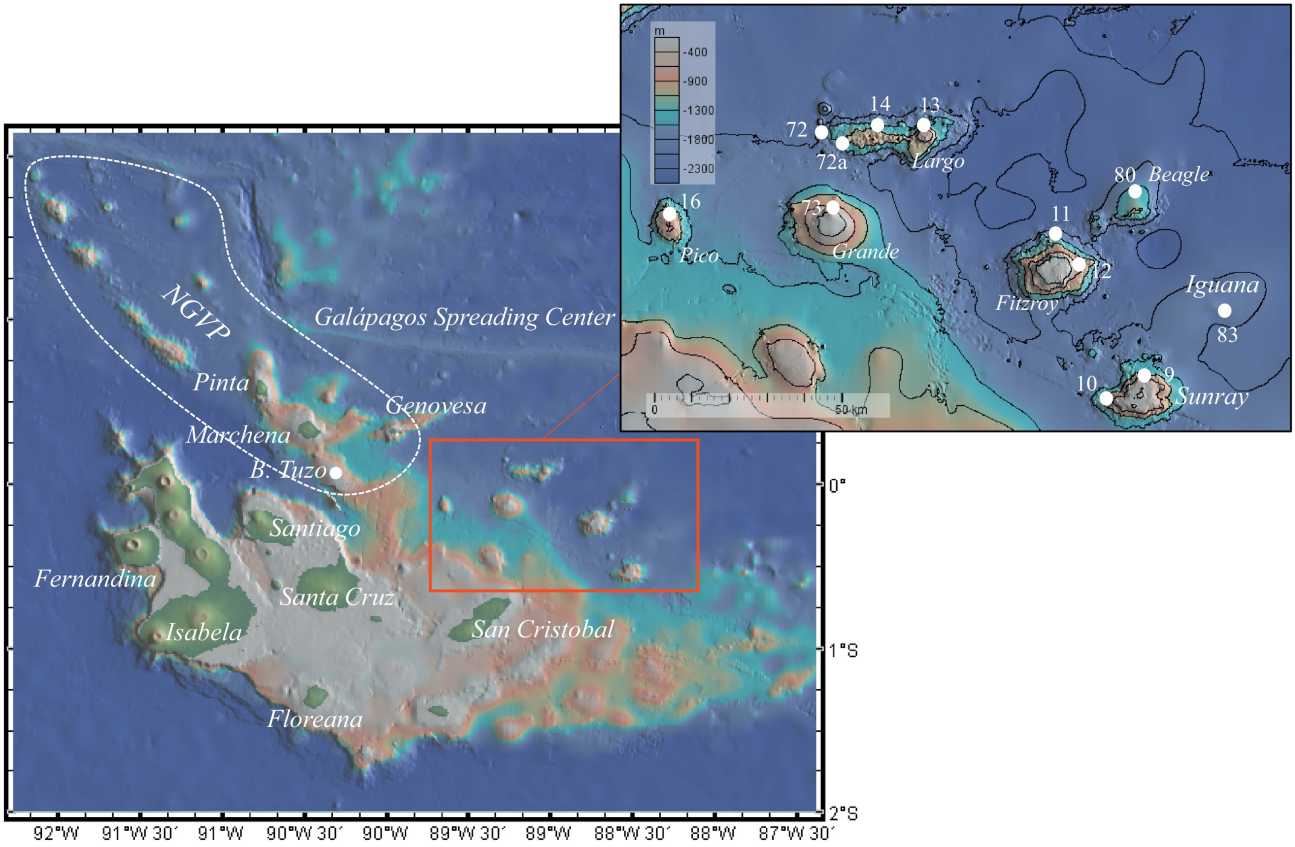
m
-400
-900
-1300
-1800
-2300
0
50 km
72
14
13
72a
Largo
16
73
Pico
Grande
80
Beagle
11
12
Fitzroy
Iguana
83
10
9
Sunray
NGVP
Galápagos Spreading Center
Pinta
Genovesa
Marchena
B. Tuzo
Santiago
Fernandina
Santa Cruz
Isabela
San Cristobal
Floreana
0°
1°S
2°S
92°W
91°W 30´
91°W
90°W 30´
90°W
89°W 30´
89°W
88°W 30´
88°W
87°W 30´

Figure 1

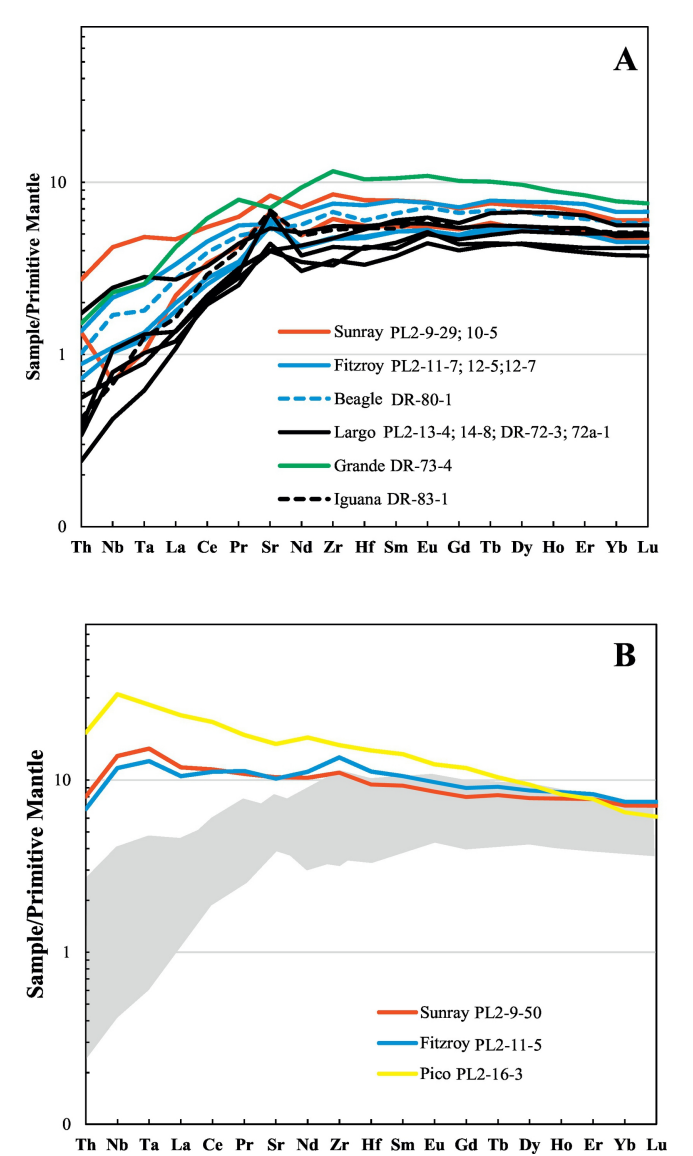
A
Sample/Primitive Mantle
10
1
0
Sunray PL2-9-29; 10-5
Fitzroy PL2-11-7; 12-5;12-7
Beagle DR-80-1
Largo PL2-13-4; 14-8; DR-72-3; 72a-1
Grande DR-73-4
Iguana DR-83-1
Th Nb Ta La Ce Pr Sr Nd Zr Hf Sm Eu Gd Tb Dy Ho Er Yb Lu
B
Sample/Primitive Mantle
10
1
0
Sunray PL2-9-50
Fitzroy PL2-11-5
Pico PL2-16-3
Th Nb Ta La Ce Pr Sr Nd Zr Hf Sm Eu Gd Tb Dy Ho Er Yb Lu

Figure 2

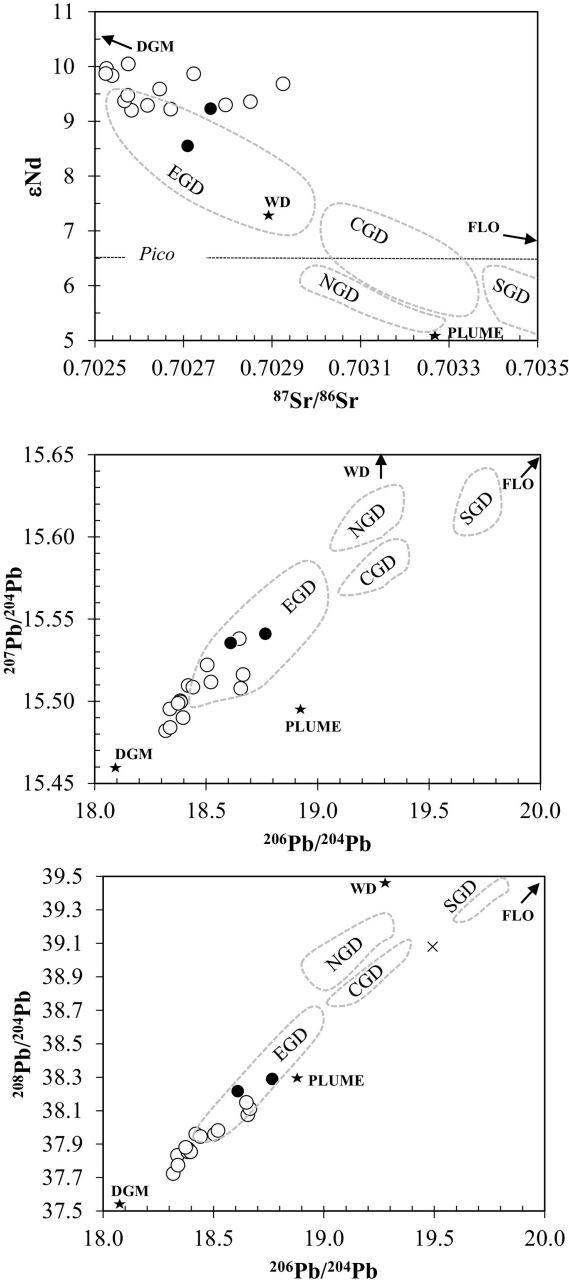
εNd
87Sr/86Sr
DGM
EGD
WD
CGD
FLO
Pico
NGD
SGD
PLUME
207Pb/204Pb
206Pb/204Pb
208Pb/204Pb

Figure 3

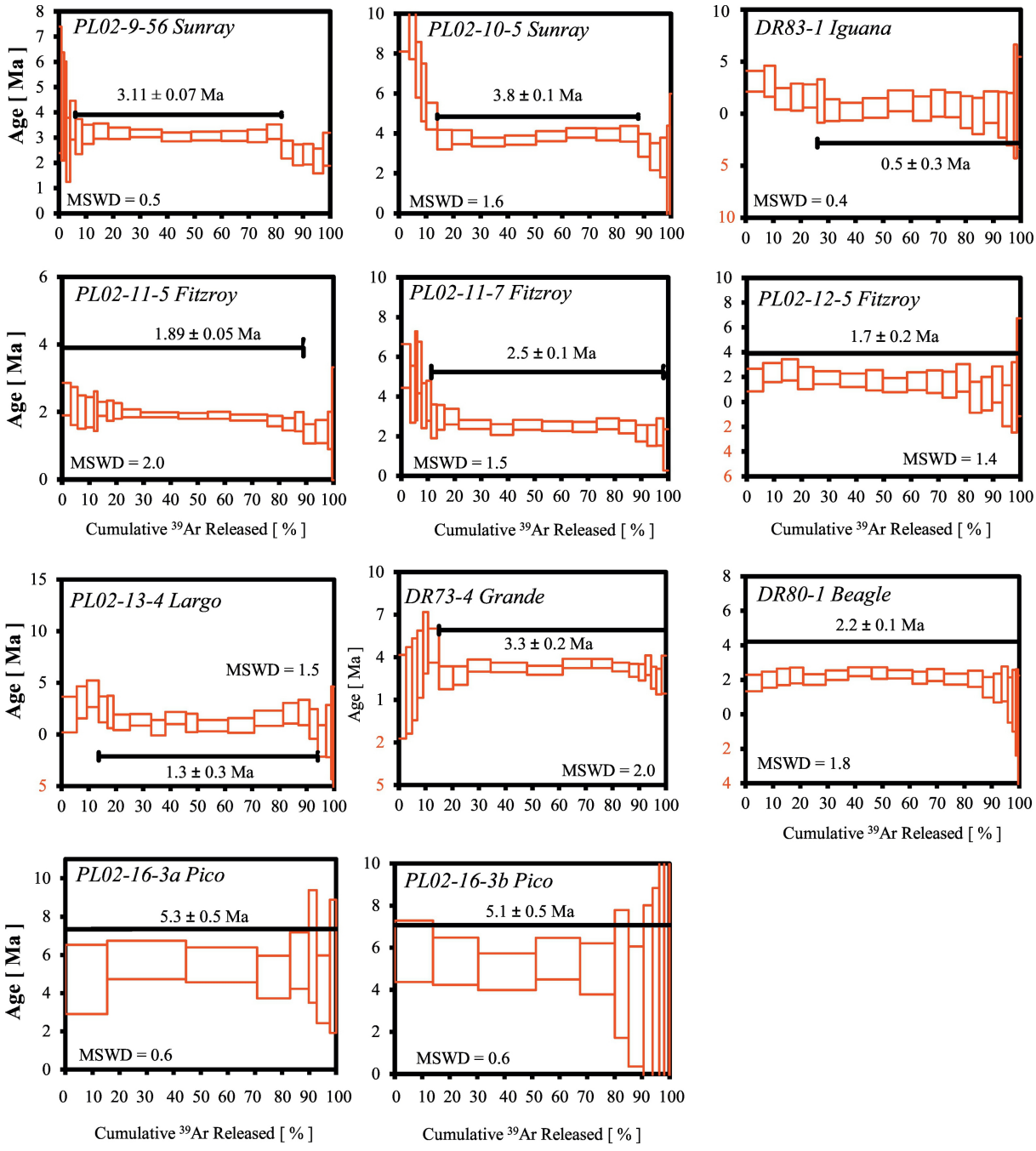
PL02-9-56 Sunray
3.11 ± 0.07 Ma
MSWD = 0.5
PL02-10-5 Sunray
3.8 ± 0.1 Ma
MSWD = 1.6
DR83-1 Iguana
0.5 ± 0.3 Ma
MSWD = 0.4
PL02-11-5 Fitzroy
1.89 ± 0.05 Ma
MSWD = 2.0
PL02-11-7 Fitzroy
2.5 ± 0.1 Ma
MSWD = 1.5
PL02-12-5 Fitzroy
1.7 ± 0.2 Ma
MSWD = 1.4
PL02-13-4 Largo
MSWD = 1.5
1.3 ± 0.3 Ma
DR73-4 Grande
3.3 ± 0.2 Ma
MSWD = 2.0
DR80-1 Beagle
2.2 ± 0.1 Ma
MSWD = 1.8
PL02-16-3a Pico
5.3 ± 0.5 Ma
MSWD = 0.6
PL02-16-3b Pico
5.1 ± 0.5 Ma
MSWD = 0.6
Age [Ma]
Cumulative 39Ar Released [%]

Figure 4

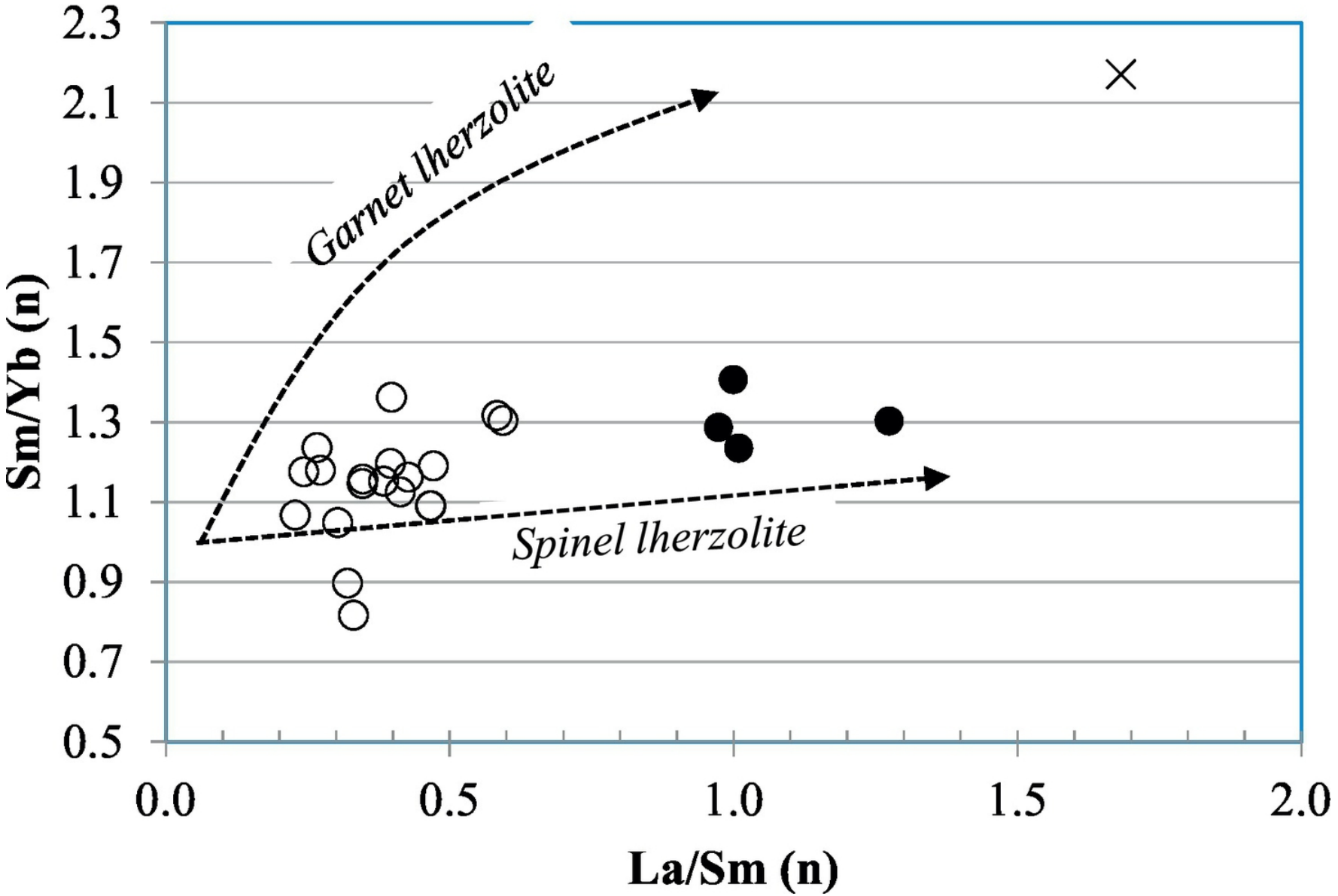
2.3
2.1
1.9
1.7
1.5
1.3
1.1
0.9
0.7
0.5
Sm/Yb (n)
Garnet lherzolite
Spinel lherzolite
0.0
0.5
1.0
1.5
2.0
La/Sm (n)

Figure 5

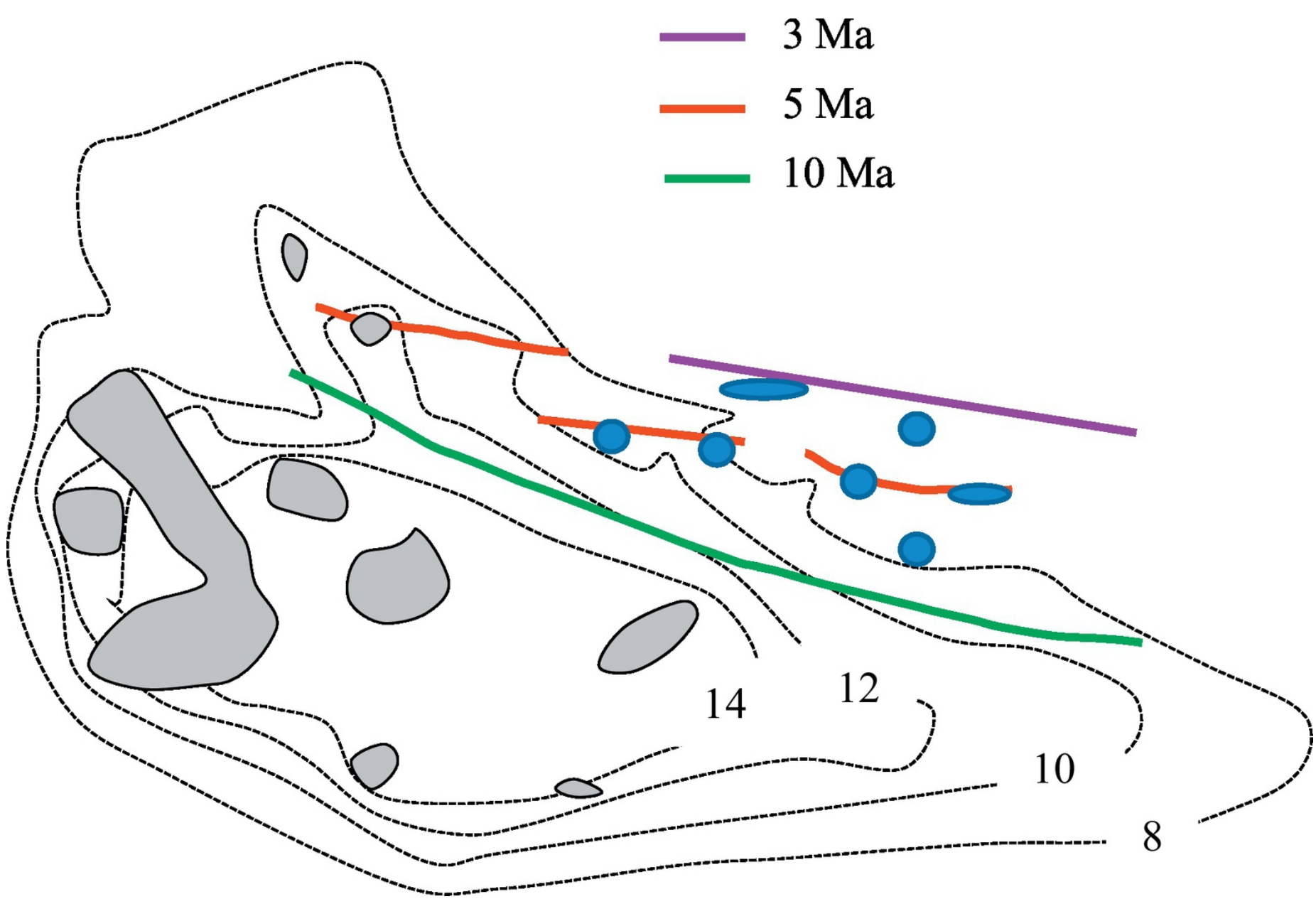

Figure 6

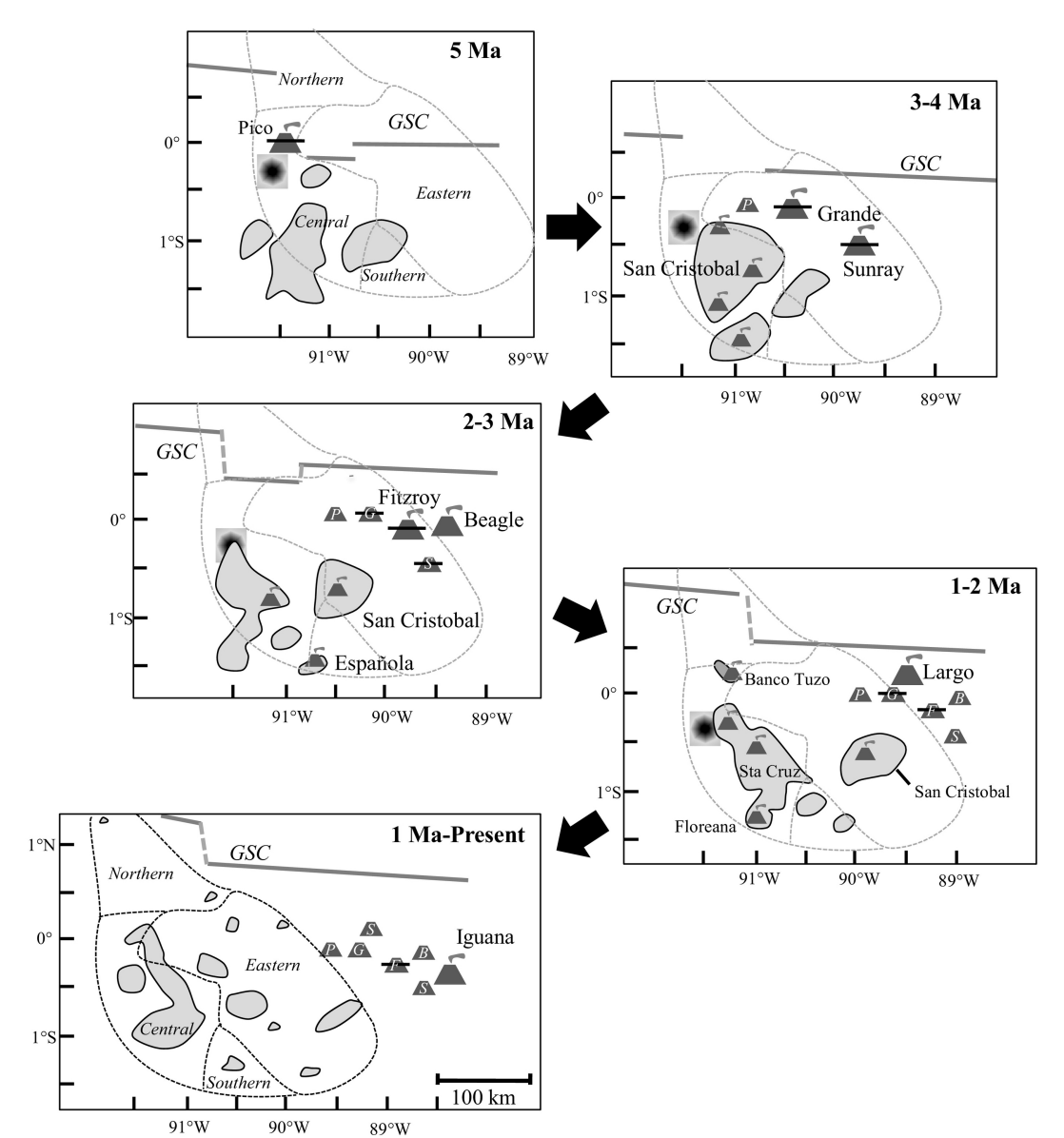
5 Ma
Northern
Pico
GSC
Eastern
Central
Southern
0°
1°S
91°W
90°W
89°W
3-4 Ma
GSC
Grande
Sunray
San Cristobal
2-3 Ma
GSC
Fitzroy
Beagle
San Cristobal
Española
1-2 Ma
GSC
Banco Tuzo
Largo
Sta Cruz
San Cristobal
Floreana
1 Ma-Present
1°N
GSC
Northern
Eastern
Central
Southern
Iguana
100 km

Figure 7

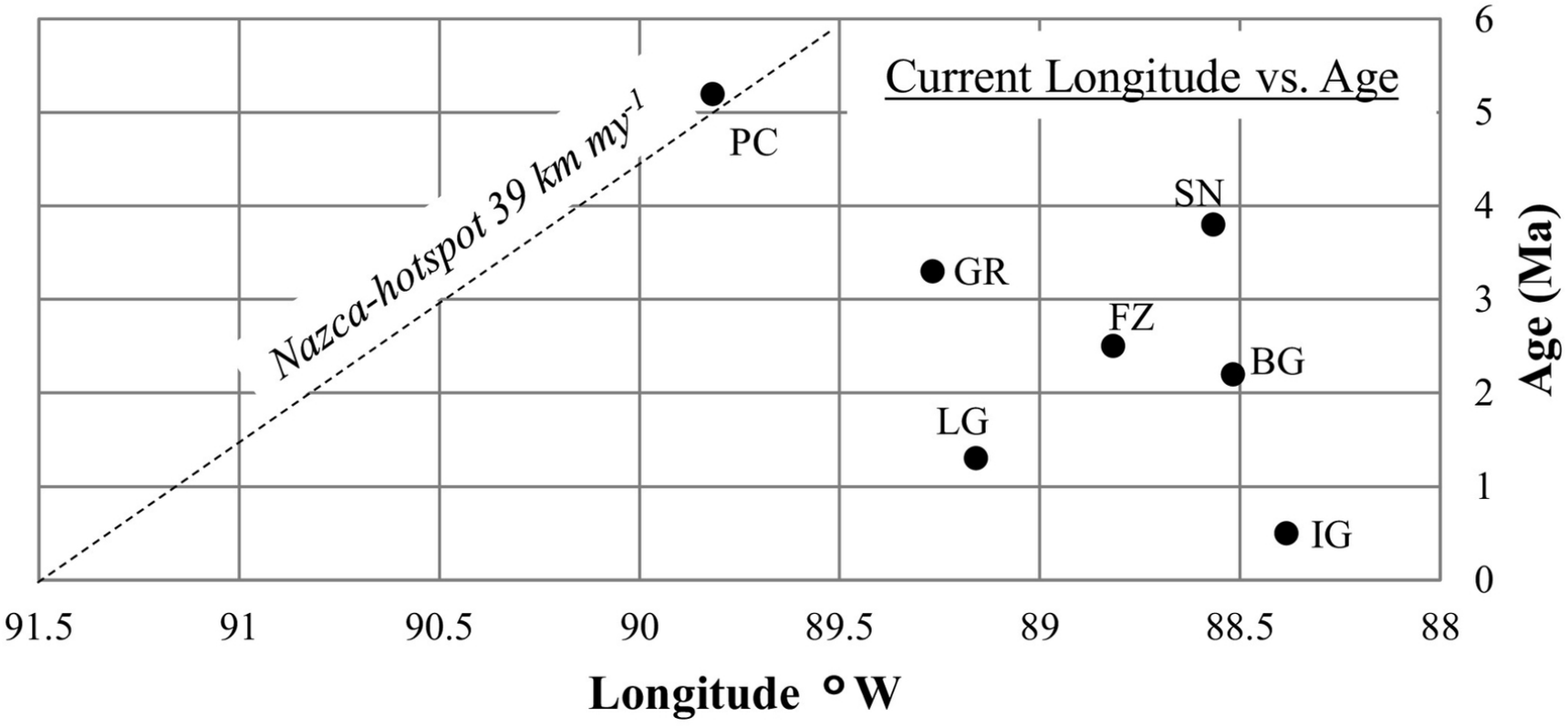
Current Longitude vs. Age
Nazca-hotspot 39 km my-1
PC
SN
GR
FZ
BG
LG
IG
91.5
91
90.5
90
89.5
89
88.5
88
Longitude °W
0
1
2
3
4
5
6
Age (Ma)

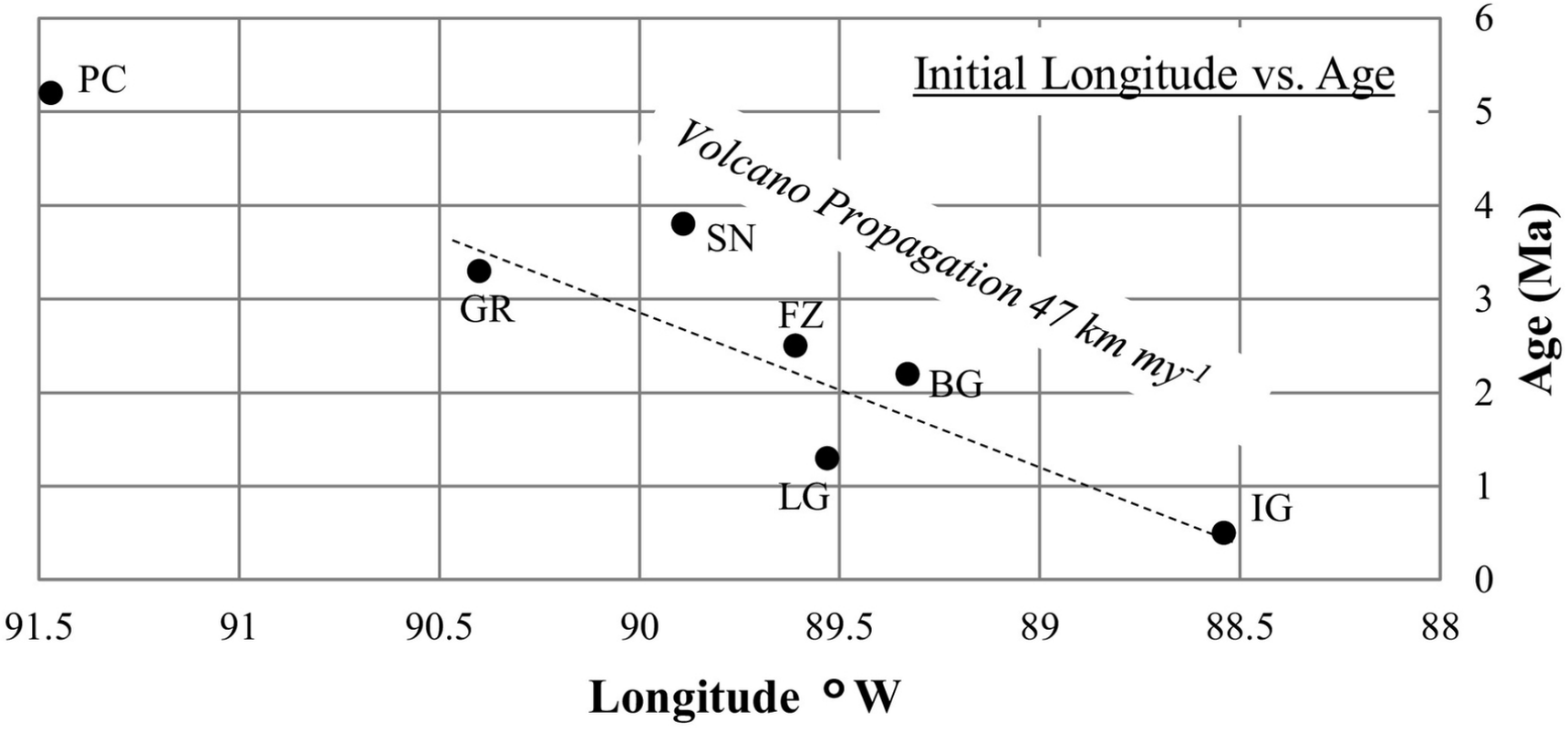
Initial Longitude vs. Age
Volcano Propagation 47 km my-1
PC
SN
GR
FZ
BG
LG
IG
91.5
91
90.5
90
89.5
89
88.5
88
Longitude °W
0
1
2
3
4
5
6
Age (Ma)

Figure 8